Shivani Sidhar
Regulatory Case Manager
San Diego Gas and Electric Company
8330 Century Park Court
San Diego, CA 92123-1530

October 5, 2016

Sent Via Electronic Mail

A.15-09-010
Wildfire Expense Memorandum Account

Mr. Don Kelly
Utility Consumers' Action Network
3405 Kenyon Street Suite 401
San Diego, CA 92110

Re: SDG&E Response to UCAN Data Request 05 - WEMA

Dear Mr. Kelly:

Attached please find SDG&E's response to UCAN Data Request 5 (UCAN-SDG&E-A.15-09-010-5), dated September 21, 2016. SDG&E's response includes general objections, narrative responses and attachments.

If you have any questions or require additional information, please feel free to contact me by phone at (858) 637-7914 or e-mail: SSidhar@semprautilities.com.

Sincerely,

Signed

Shivani Sidhar
Regulatory Case Manager

Enclosures

cc: Chris Lyons – SDG&E
Stacie Atkinson – SDG&E

UCAN DATA REQUEST
UCAN-SDG&E DR-05, Q1-5
SDG&E WEMA PROCEEDING - A.15-09-010
SDG&E RESPONSE
DATE RECEIVED: September 21, 2016
DATE RESPONDED: October 5, 2016

I. GENERAL OBJECTIONS

1. SDG&E objects generally to each request to the extent that it seeks information protected by the attorney-client privilege, the attorney work product doctrine, statutory mediation confidentiality (see Cal. Evid. Code §§ 1115-28) or any other applicable privilege or evidentiary doctrine. No information protected by such privileges will be knowingly disclosed.

2. SDG&E objects generally to each request that is overly broad and unduly burdensome. As part of this objection, SDG&E objects to discovery requests that seek "all documents" or "each and every document" and similarly worded requests on the grounds that such requests are unreasonably cumulative and duplicative, fail to identify with specificity the information or material sought, and create an unreasonable burden compared to the likelihood of such requests leading to the discovery of admissible evidence. Notwithstanding this objection, SDG&E will produce all relevant, non-privileged information not otherwise objected to that it is able to locate after reasonable inquiry.

3. SDG&E objects generally to each request to the extent that the request is vague, unintelligible, or fails to identify with sufficient particularity the information or documents requested and, thus, is not susceptible to response at this time.

4. SDG&E objects generally to each request that: (1) asks for a legal conclusion to be drawn or legal research to be conducted on the grounds that such requests are not designed to elicit facts and, thus, violate the principles underlying discovery; (2) requires SDG&E to do legal research or perform additional analyses to respond to the request; or (3) seeks access to counsel's legal research, analyses or theories.

5. SDG&E objects generally to each request to the extent it seeks information or documents that are not reasonably calculated to lead to the discovery of admissible evidence.

6. SDG&E objects generally to each request to the extent that it is unreasonably duplicative or cumulative of other requests.

7. SDG&E objects generally to each request to the extent that it would require SDG&E to search its files for matters of public record such as filings, testimony, transcripts, decisions, orders, reports or other information, whether available in the public domain or through FERC or CPUC sources.

8. SDG&E objects generally to each request to the extent that it seeks information or documents that are not in the possession, custody or control of SDG&E.

9. SDG&E objects generally to each request to the extent that the request would impose an undue burden on SDG&E by requiring it to perform studies, analyses or calculations or to create documents that do not currently exist.

10. SDG&E objects generally to each request that calls for information that contains trade secrets, is privileged or otherwise entitled to confidential protection by reference to statutory protection. SDG&E objects to providing such information absent an appropriate protective order. With respect to the Office of Ratepayer Advocates, however, SDG&E will produce such information subject to the requirements of Public Utilities Code Section 583 and General Order 66-C.

II. EXPRESS RESERVATIONS

1. No response, objection, limitation or lack thereof, set forth in these responses and objections shall be deemed an admission or representation by SDG&E as to the existence or nonexistence of the requested information or that any such information is relevant or admissible.

2. SDG&E reserves the right to modify or supplement its responses and objections to each request, and the provision of any information pursuant to any request is not a waiver of that right.

3. SDG&E reserves the right to rely, at any time, upon subsequently discovered information.

4. These responses are made solely for the purpose of this proceeding (A.15-09-010) and for no other purpose.

UCAN DATA REQUEST
UCAN-SDG&E DR-05, Q1-5
SDG&E WEMA PROCEEDING - A.15-09-010
SDG&E RESPONSE
DATE RECEIVED: September 21, 2016
DATE RESPONDED: October 5, 2016

III. RESPONSES

Request 1:

Have any meteorological data (this includes but is not limited to surface station data or atmospheric re-analyses) been introduced into Dr. Peterka's modeling simulations through techniques such as, but not limited to, nudging or other methods of data assimilation?

Objection: SDG&E objects to this request on the grounds set forth in General Objection 3. Subject to the foregoing objection, SDG&E responds as follows.

Response:

In the mesoscale modeling, nudging was only used at domain level 1. No meteorological data or nudging was used at domain levels 2 and 3.

UCAN DATA REQUEST
UCAN-SDG&E DR-05, Q1-5
SDG&E WEMA PROCEEDING - A.15-09-010
SDG&E RESPONSE
DATE RECEIVED: September 21, 2016
DATE RESPONDED: October 5, 2016

Request 2:

For Dr. Peterka's modeling as described in his direct testimony, have any meteorological data (this includes but is not limited to surface station data or atmospheric re-analyses) been introduced into the modeling simulations to adjust simulation results after they are complete (other than the post-simulation adjustments in the numerical simulations carried out by Dr. Peterka and described in his direct testimony of 9/25/15 on p. 12 Lines 1-5)?

Objection: SDG&E objects to this request on the grounds set forth in General Objection 3. Subject to the foregoing objection, SDG&E responds as follows.

Response:

No.

UCAN DATA REQUEST
UCAN-SDG&E DR-05, Q1-5
SDG&E WEMA PROCEEDING - A.15-09-010
SDG&E RESPONSE
DATE RECEIVED: September 21, 2016
DATE RESPONDED: October 5, 2016

Request 3:

Regarding Mr. Vanderburg's wind speed analysis that used historical weather data (as described above) to fine tune the forecast models, have any meteorological data (this includes but is not limited to surface station data or atmospheric re-analyses) been introduced to adjust the findings after the analysis has been complete? If so, please explain

Objection: SDG&E objects to this request on the grounds set forth in General Objection 3. Subject to the foregoing objection, SDG&E responds as follows.

Response:

No. See the attached paper titled "sawti_explained.pdf" (Rolinski et al.) for details. This paper has been accepted for publication in the American Meteorological Society's Journal of Weather and Forecasting.

UCAN DATA REQUEST
UCAN-SDG&E DR-05, Q1-5
SDG&E WEMA PROCEEDING - A.15-09-010
SDG&E RESPONSE
DATE RECEIVED: September 21, 2016
DATE RESPONDED: October 5, 2016

Request 4:

Please describe what historical weather data was used to fine tune the weather forecast models referenced by Mr. Vanderburg on page 8, lines 3-4 of his direct testimony. Please also describe how that information was used to fine tune the weather forecast models.

Response:

The attached published paper by Yang Cao and Robert Fovell addresses the answer to these two questions in great detail. To clarify, "fine tuning" refers to the process of identifying the best possible configuration of WRF (Weather Research and Forecasting model) with regards to Santa Ana wind forecasts. The following is an excerpt from the attached paper (page 530).

> "Model forecasts are verified against wind observations reported by the SDG&E mesonet, a recently installed and exceptionally dense surface observing network of (presently) more than 140 stations sited primarily in well-exposed, wind-prone areas on the west-facing slopes of the county's mountains. Numerous combinations of model physical parameterizations were examined, for this and similar events, to identify the configuration that best captures the magnitude, temporal evolution, and spatial extent of the winds."

UCAN DATA REQUEST
UCAN-SDG&E DR-05, Q1-5
SDG&E WEMA PROCEEDING - A.15-09-010
SDG&E RESPONSE
DATE RECEIVED: September 21, 2016
DATE RESPONDED: October 5, 2016

Request 5:

Please identify the magnitude of the tuning factors described by Vanderburg to adjust the high resolution weather forecast models and describe any spatial or temporal variability in their application.

Response:

See response to Request 4 above.

Attachment: sawti_explained (Rolinski et al)

The Santa Ana Wildfire Threat Index: Methodology and Operational Implementation

Tom Rolinski* and Scott B. Capps

University of California, Los Angeles, CA, USA

Robert G. Fovell

University of California, Los Angeles, CA, USA

Yang Cao

University of California, Los Angeles, CA, USA

Brian J. D'Agostino

San Diego Gas & Electric, San Diego, CA, USA

Steve Vanderburg

San Diego Gas & Electric, San Diego, CA, USA

Corresponding author address: Tom Rolinski, United States Forest Service, 2524 Mulberry St., Riverside, CA 92501.

E-mail: thomasrolinski@fs.fed.us

ABSTRACT

Santa Ana winds, common to Southern California during the fall through early spring, are a type of downslope windstorm originating from a direction generally ranging from 360°/0° to 100° and is usually accompanied by very low humidity. Since fuel conditions tend to be driest from late September through the middle of November, Santa Ana winds occurring during this time have the greatest potential to produce large, devastating fires upon ignition. Such catastrophic fires occurred in 1993, 2003, 2007, and 2008. Because of the destructive nature of such fires, there has been a growing desire to categorize Santa Ana wind events in much the same way that tropical cyclones have been categorized. The Santa Ana Wildfire Threat Index (SAWTI) is an index that categorizes Santa Ana wind events with respect to anticipated fire potential. The latest version of the index has been a result of a three and a half year collaboration effort between the USDA Forest Service, the San Diego Gas and Electric utility (SDG&E), and the University of California, Los Angeles (UCLA). SAWTI uses several meteorological and fuel moisture variables at 3 km resolution using the Weather Research and Forecasting (WRF) model to generate the index out to 6 days. In addition to the index, a 30 year climatology of weather, fuels and the SAWTI has been developed to help put current and future events into perspective. This paper outlines the methodology for developing the SAWTI, including a discussion on the various datasets employed and its operational implementation.

1. Introduction

From the fall through early spring, offshore winds, or what are commonly referred to as Santa Ana winds, occur over Southern California from the coastal mountains westward, from Ventura County southward to the Mexican border. These synoptically driven wind events vary in frequency, intensity, and spatial coverage from month to month and from year to year, thus making them difficult to categorize. Most of these wind events are associated with mild to warm ambient surface temperatures $\geq 18\,^{\circ}\mathrm{C}$ and low surface relative humidity $\leq 20\,\%$. However, during the late fall and winter months, these events tend to be associated with lower surface temperatures due to the air mass over the Great Basin originating from higher latitudes and other seasonal effects. There are a variety of ways to define a Santa Ana event through the analysis of local and synoptic scale surface pressure and thermal distributions across Southern California (Raphael 2003). We view these offshore winds from a wildfire potential perspective, taking into consideration both the fuel characteristics and weather. As we have found, the index discussed herein provides a robust descriptor of both Santa Ana Winds and the potential for wildfire activity. Used in conjunction with a Mean Sea Level Pressure (MSLP) map type, this is a powerful method to separate Santa Ana Wind events from the more typical nocturnal offshore flows that occur throughout the coastal and valley areas (i.e, land breeze) during the year.

From October 21^{st} through the 23^{rd}, 2007, Santa Ana winds generated multiple large catastrophic fires across Southern California (Moritz et al. 2010). Most notable was the Witch Creek fire in San Diego County, where wind gusts of $26\,\mathrm{m\,s^{-1}}$ were observed at the Julian weather station along with relative humidity values of $\approx 5\,\%$. However, high resolution model simulations at 667 m showed that wind velocities were much higher in unsampled areas (Cao and Fovell 2016). This event became the catalyst for the development of a comprehensive Santa Ana wildfire poten-

tial index to better inform fire agencies, first responders, private industry, and the general public about the severity of an approaching event. This index could also help augment Fire Weather Watches and Red Flag Warnings from the National Weather Service by providing value added information about an impending event.

The Predictive Services Unit, functioning out of the Geographic Area Coordination Center (GACC) in Riverside, California, is comprised of several meteorologists employed by the USDA Forest Service. In 2009, Predictive Services began working on an index that categorizes Santa Ana wind events according to the potential for a large fire to occur (Rolinski et al. 2011). This unique approach addresses the main impact Santa Ana winds can have on the population of Southern California beyond the causal effects of windy, dry weather. Following on, and improving upon this work, the Forest Service (through Predictive Services) collaborated during a three and a half year period with the San Diego Gas and Electric utility (SDG&E) and the University of California, Los Angeles (UCLA) to develop the Santa Ana Wildfire Threat Index (SAWTI). This index employs a gridded 3 km model to not only assess meteorological conditions, it also incorporates an estimation of fuel moisture to determine the likelihood of rapid fire growth during Santa Ana winds.

The SAWTI domain covers the coastal, valley, and mountain areas of Southern California from Point Conception southward to the Mexican border. This area has been divided into 4 zones based in part on the different offshore flow characteristics that occur across the region (Figure 1). Zone 4, which covers Santa Barbara County and was the last zone to be included into the index (thus the reason for the discontinuity within the sequential order of zones going from north to south), does not typically experience Santa Ana winds in the classic sense. Strong northwest to north winds in this zone can either precede a Santa Ana wind event or can occur independently (typically in the summer), which in the latter case are more commonly known as“Sundowners”

(Blier 1998). In both cases, these downsloping winds are common to the south slopes of the Santa Ynez Mountains, an east-west coastal range which runs parallel to, and a few miles inland from the shoreline. Although not frequent, significant fire activity associated with these winds in this zone has occurred in the past which is why this geographic area is now represented in the index. Santa Ana winds across zones 1 and 2 are primarily a result of offshore surface pressure gradients (locally and/or synoptically) interacting with the local terrain to produce gap winds through the Soledad Canyon, the Cajon Pass, and the Banning Pass (Hughes and Hall 2010; Cao and Fovell 2016). These winds also tend to precede the Santa Ana winds that occur across San Diego County by 12 to 24 hours. Across zone 3, offshore winds take on a more "downslope windstorm" characteristic driven largely by the tropospheric stability (Cao and Fovell 2016). Other factors that led to the division of zones were changes in terrain, National Weather Service Forecast Office boundaries, and local news media market areas. The SAWTI is more than a tool for meteorologists and fire agency managers to assess the severity of Santa Ana winds; it is also a tool for the general public to help better prepare for impending events that could lead to catastrophic fires. Therefore, the idea of displaying the product via zones keeps the index simple and easy to understand for all user groups. The following discussion centers around the assessment of fire potential related to Santa Ana winds, the methodology behind the weather and fuel components of the index, and its operational implementation.

2. Methodology

a. Large Fire Potential - Weather Component

We define a large fire within the four SAWTI zones to be 100 hectares. The potential for an ignition to reach or exceed this value depends on a number of components: e.g., various meteorological

and fuel conditions, suppression strategy, topography, accessibility, and resource availability. We achieved this threshold by employing a historical fire database that was constructed by Predictive Services. This database was assembled by collecting fire occurrence data (1990-2013) from all state and federal fire agencies within the confines of California. For example, some of the fire agencies include the USDA Forest Service, the Bureau of Land Management, the National Park Service, and CALFIRE to mention a few. This database contains information such as ignition date, acres burned, containment date, etc., and contains $32,683$ records. The value of 100 hectares was achieved by determining what the largest fire was for each day within the database and then taking the 95^{th} percentile of all daily largest fires. The determination of this semi-empirical threshold was also guided by decades of experience guiding coordinated attacks on wildfires throughout Southern California. Moreover, in most cases when this threshold is exceeded, the GACC becomes engaged in resource mobilization to assist in fire suppression. Current methods to evaluate fire potential include various indices from the National Fire Danger Rating System (NFDRS, (Bradshaw et al. 1983)) and from the Canadian Forest Fire Danger Rating System (CFFDRS) (Preisler et al. 2008). The Fosberg Fire Weather Index (FFWI) is one such index which is a function of wind speed, humidity, and temperature with output values ranging from 0 to 100 (Fosberg 1978). While the FFWI may show elevated output values for a Santa Ana wind event, it can also show elevated values for *any* day therefore making it too generic for our purposes.

Assuming an aggressive suppression strategy is employed with adequate resource availability in an easily accessible area; Large Fire Potential (LFP) can be simplified into a function involving fuel and meteorological conditions preceding, during, and following the time of ignition. From observation and experience, the two weather variables that contribute most toward fire growth during a Santa Ana wind event are wind velocity and the amount of dry air present near the surface. To illustrate this concept, we examined the difference between two Southern California

fire regimes (Jin et al. 2015) consisting of fire activity during the summer, versus only during the fall when Santa Ana winds begin to increase in frequency (Figures 2 and 3). It is easy to see that most of the fire activity during the summer occurs in low wind situations with varying dewpoint depression values. However, fires burning in the autumn, are commonly associated with stronger winds and higher dew point depression values. Therefore, based on operational experience, observations, and model data, we believe the potential for a new ignition to reach or exceed 100 hectares based solely on weather conditions during a Santa Ana wind event, is best expressed by the following equation:

$$\mathrm{LFP_w} = 0.001 \mathrm{W_s}^2 \mathrm{D_d} \tag{1}$$

where $\mathrm{W_s}$ is the near surface (10 m AGL) sustained wind speed (mph), and $\mathrm{D_d}$ is the near surface dew point depression (°F). It should be noted that this equation was validated by examining dynamically downscaled reanalysis data across Southern California for the month of October from 1979 to 2010. It has been suggested that wind speed has an exponential effect on the spread of fire among finer fuels such as grass and brush, and that wind can also have the same effect on fire spread as a fire burning upslope with little or no wind (Rothermel 1972). Dew point depression (T–T_d) depicts the dryness at the surface well, and affects the moisture content of vegetation. Also, dew point depression can sometimes differentiate better between warm and cold offshore events than relative humidity can. In our dataset, it has been noted that larger dew point depression values ($\mathrm{D_d} \geq 24\,^{\circ}\mathrm{C}$) have mainly been associated with warm events. While this may seem trivial, cold Santa Ana wind events (surface ambient temperatures $< 16\,^{\circ}\mathrm{C}$) are usually not associated with large fires (according to our historical fire database previously mentioned). This may be due in part to lower fuel temperatures because in those cases more time would be needed to reach the ignition temperature. Another reason is that colder events are sometimes preceded by

precipitation either by a few days or by a few weeks which would cause fuels to be less receptive to new ignitions. These are the primary reasons why temperature was excluded from (1), although it has been incorporated indirectly through the use of D_d, and in the fuels component that will be discussed in the following section. Finally, we note that while (1) bears some resemblance to the FFWI, a comparison of daily outputs of FFWI and LFP_w revealed that LFP_w provides significantly greater contrast between Santa Ana days and non-Santa Ana days. Therefore, these results favored LFP_w as being the more appropriate equation for our purpose.

b. Large Fire Potential - Fuel Moisture Component

In addition to the meteorological conditions, LFP is also highly dependent on the state of the fuels. Given the complexity of the fuel environment (i.e., fuel type, continuity, loading, etc.), we decided to focus more specifically on fuel moisture since that aspect plays a critical role in the spread of wildfires (Chuvieco et al. 2004). For our purpose, we have condensed fuel moisture into three parameters: 1) dead fuel moisture, 2) live fuel moisture, and 3) the state of green-up of the annual grasses. Each of these aspects of fuel moisture is complex and will be defined more specifically later. We combined these moisture variables into one term which we refer to as the Fuel Moisture Component (FMC). While the variables within FMC often act in concert with each other, there are times when they are out of phase with one another due to the variability in precipitation (frequency and amount) that occurs across Southern California during the winter. Through a comprehensive empirical investigation, the governing equation for FMC can be expressed as follows:

$$\mathrm{FMC} = \left[0.1\left(\left(\frac{\mathrm{DL}}{\mathrm{LFM}} - 1\right) + \mathrm{G_{ag}}\right)\right]^{1.7} \tag{2}$$

where DL is the Dryness Level consisting of the Energy Release Component (ERC) and the 10 hour dead fuel moisture time lag (DFM_{10hr}). Dead fuel refers to non-living plant material whose

moisture content responds only to ambient moisture. Dead fuel is typically grouped into "time-lag" classes according to diameter as follows: 0.20 cm (DFM_{1hr}), 0.64 cm (DFM_{10hr}), 2.00 cm (DFM_{100hr}) and 6.40 cm (DFM_{1000hr}). Live Fuel Moisture (LFM) is a sampling of the moisture content of the live fuels indigenous to the local region, and G_{ag} is the degree of green-up of the annual grasses. Currently we are making the assumption that all the terms in (2) have equal weight, but further study may lead to future modification.

1) Dryness Level

The DL is a function of ERC and DFM_{10hr} calibrated to historical fire occurrence across Southern California with unitless values ranging from 1 to 3. ERC is a relative index of the amount of heat released per unit area in the flaming zone of an initiating fire and is comprised of live and dead fuel moisture as well as temperature, humidity, and precipitation (Bradshaw et al. 1983). While ERC is a measure of potential energy, it also serves to capture the intermediate to long term dryness of the fuels with unitless values generally ranging from 0–100 (using NFDRS fuel model G). The DFM_{10hr} represents fuels in which the moisture content is exclusively controlled by environmental conditions (Bradshaw et al. 1983). Output values of DFM_{10hr} are in g/g expressed as a percentage ranging from 0–60. In the case of the DFM_{10hr}, this is the time required for dead fuels (0.64–2.54 cm in diameter) to lose approximately two-thirds of their initial moisture content (Bradshaw et al. 1983). Thus a DL of 1 indicates that dead fuels are moist, 2 represents average dead fuel dryness, and a 3 indicates that the dead fuels are drier than normal.

2) Live Fuel Moisture (LFM)

The observed LFM is the moisture content of live fuels, e.g., grasses, shrubs, and trees, expressed as a ratio of the weight of water in the fuel sample to the oven dry weight of the fuel sample (Pollet

and Brown 2007). Soil moisture as well as soil and air temperature govern the physiological activity which results in changes in fuel moisture (Pollet and Brown 2007). LFM is a difficult parameter to evaluate because of the irregularities associated with observed values. For instance, samples of different species of native shrubs are normally taken twice a month by various fire agencies across Southern California. However, the sample times often differ between agencies and the equipment used to dry and weigh the samples may vary from place to place. In addition, sample site locations are irregular in distribution and observations from these sites may be taken sporadically. This presents a problem when we attempt to assess LFM over the region shown in Figure 1.

Apart from taking fuel samples, there are several ways of estimating LFM using meteorological variables, soil water reserve, solar radiation, etc. (Castro et al. 2003). In particular, we developed an approach to modeling the LFM of chamise or greasewood (*Adenostoma fasciculatum*), a common shrub that grows within the chaparral biome in Southern California and is particularly flammable due to its fine, needle-like leaves and other characteristics (Countryman and Philpot 1970; Fovell et al. 2016). This strategy makes use of historical observed LFM data from 10 sampling sites across Southern California and soil moisture from the 40–100 cm layer ($\mathrm{SMOIS}_{40-100\mathrm{cm}}$) from the North American Land Data Assimilation System, Phase 2 (NLDAS–2). At each sampling site, LFM deviations from climatology are predicted using $\mathrm{SMOIS}_{40-100\mathrm{cm}}$ departures from its own annual cycle. A key element of the model is the incorporation of a 22 day lag between $\mathrm{SMOIS}_{40-100\mathrm{cm}}$ and LFM which improved the model fits. This is because a certain period of time elapses during which water percolates downward through the soil layers and then is drawn back up through the root system of the plant. This time can vary between 4 and 43 days depending on the evaporative conditions, soil structure, and site elevation. An average of this time-

lag over all the stations equated to 22 days. LFM observed now is relatable to gridded NLDAS–2 soil moisture anomalies from about three weeks earlier.

That approach, although quite skillful, results in site-specific equations not easily generalized across Southern California. The SAWTI index presently makes use of a simplified version of this strategy, applied to all grid points in the domain. For a given day, the model can be expressed as follows:

$$\text{LFM} = \left(\text{SMOIS}_{40-100\text{cm }22\text{days}} - \text{SMOIS}_{\text{m}}\right) + 82, \tag{3}$$

where $\text{SMOIS}_{40-100\text{cm }22\text{days}}$, is the soil moisture of the 40–100 cm layer from 22 days earlier, and SMOIS_{m}, is the mean soil moisture from 2009 to 2012 for that same date. The empirically selected constant of 82 roughly approximates the annual mean LFM over a large variety of sites.

3) Annual Grasses (G_{ag})

Following the onset of significant wetting rains, new grasses will begin to emerge in a process called green-up. While the timing and duration of this process fluctuates from year to year, some degree of green-up usually occurs by December across Southern California. During the green-up phase, grasses will begin to act as a heat sink, thereby preventing new ignitions and/or significantly reducing the rate of spread among new fires. By late spring these grasses begin to cure with the curing phase normally completed by mid-June. In (2), G_{ag} is a value that quantifies the said green-up and curing cycles of annual grasses.

G_{ag} is derived from the Moderate Resolution Imaging Spectroradiometer (MODIS) NDVI data at a resolution of 250 meters for select pixels consisting solely of grasslands. NDVI is further defined by red and near-infrared (NIR) bands in the following equation:

$$\text{NDVI} = \frac{\rho_{\text{NIR}} - \rho_{\text{b}}}{\rho_{\text{NIR}} + \rho_{\text{b}}} \tag{4}$$

where b is the reflectance in band b (Clinton et al. 2010). It can be shown that NDVI values for Southern California grasslands generally range from about 0.25 ($\pm$0.05) to 0.75 ($\pm$0.05) for an average rainfall year (Figure 4). There is evidence that NDVI is affected by soil color (Elmore et al. 2000), which may explain the NDVI differences ($\pm$0.05) seen among the selected Southern California grassland locations.

G_{ag} is given a rating of 0 to 5 based on NDVI data, where 0 is green and 5 is fully cured. When applying the methodology discussed by White et al. (1997) to the general range of Southern California grasslands, green-up is estimated to have occurred when NDVI exceeds 0.50. However, we have found that this value can be closer to 0.64 for some sites, and therefore NDVI values greater than 0.64 are assigned a value of 0, or green. Furthermore, NDVI values less than or equal to 0.39 are assigned a value of 5. This is because NDVI values are observed to be below 0.39 for all grassland sites during the dry season when grasses are known to be fully cured. A linear relationship exists between NDVI-derived values of $G_{ag}$and fire occurrence in Southern California (Figure 5). For this reason, the transition between green and fully cured (or vice versa) was given a rating of 1 to 4 in NDVI increments of 0.05 (Table 1).

To model NDVI, we used MODIS-derived NDVI biweekly data observed at 21 stations shown in Figure 1, interpolated to daily frequency using cubic splines. The data availability period was January 2004-June 2012. For the ease of implementation, our goal was to create a simple, yet skillful equation to capture the temporal variation of NDVI:

$$\begin{aligned} \mathrm{NDVI} = \alpha + \beta_1 \cos(2\pi \mathrm{DOY}/\mathrm{LOY}) + \beta_2 \mathrm{PRECIP}_{\mathrm{accum}} \\ + \beta_3 \mathrm{RH}_{\mathrm{avg}} + \beta_4 \mathrm{VEG}_{\mathrm{frac}} + \beta_5 \mathrm{SMOIS}_{40-100\mathrm{cm}} \end{aligned} \tag{5}$$

where DOY = January 1st-based day of year and LOY is the length of year in days. The regressor $\mathrm{PRECIP}_{\mathrm{accum}}$ is the September 1st-based annually accumulated precipitation [mm], $\mathrm{RH}_{\mathrm{avg}}$ is the

30-day running averaged to relative humidity, $\mathrm{VEG_{frac}}$ is the surface vegetation fraction $(0-1)$, and $\mathrm{SMOIS_{40-100cm}}$ is the soil moisture content of the $40-100$ cm depth [kg/m^3]. This equation was the result of the "random forest" selection and stepwise regression applied to a large number of meteorological candidate regressors; see Cao (2015) for more information. The R^2 of the model is 0.73; see Table 2 for coefficient values.

We applied this model to the 21 sites in the four zones shown in Figure 1. It is recognized that at some stations and times, the NDVI predictions are somewhat out of phase (i.e., the up and down ramps are too early or too late) with the observations, and the peaks are over or under predicted at different locations and times. The marked drought year of 2007 is clearly a problem at some locations, especially in zone 2. However, considering the fact that this is a simple universal model with only 5 regressors applied across Southern California, we believe it has shown adequate skill overall (Cao 2015).

c. Large Fire Potential - Weather and Fuels

Given our derived expression for fuel characteristics we can now predict large fire potential during Santa Ana wind events taking into consideration both the weather and the fuels. FMC modifies (1) in cases where fuels have not fully cured and are still inhibiting fire spread. Output values of FMC range from 0 to 1, where 0 represents wet fuels and 1 denotes dry fuels. This modifier can become so influential that it will greatly reduce or even eliminate the potential for large fire occurrence despite favorable meteorological conditions for rapid fire growth. So the final equation for large fire potential becomes:

$$\mathrm{LFP} = 0.001 \mathrm{W_s}^2 \mathrm{D_d} \mathrm{FMC} \tag{6}$$

The value of the incorporation of fuel moisture predictions into the index is illustrated in Figure 6. For example, examination of the period between September 2008 and May 2009 shows a number of significant Santa Ana wind events indicated by the spikes in LFP_w. The difference between LFP_w and LFP is small during the fall months attributed to high FMC values. This is confirmed by viewing the relatively close spatial agreement between LFP_w and LFP (Figure 7). In contrast, large differences occur after significant winter rains commence (Figure 8). Large wildfires had occurred during each of the spikes noted in the fall while little fire activity was recorded despite the LFP_w spikes during January. This is precisely due to low FMC values which illustrates the critical role that fuels play in this index.

3. **Operational** SAWTI

a. Model Configuration

The data ingested to compute the four-zone, six-day LFP operational forecasts comes from multiple sources at different temporal and horizontal resolutions ranging from hourly to daily, and 3 km to 12.5 km, respectively (Figure 9). To reduce the exposure to error in fields with long accumulation periods, we sourced input variables for LFM and NDVI from the NLDAS–2 data (constructed using a land surface model in conjunction with assimilated observations and atmospheric model output). In contrast, hourly DFM and ERC values are predicted using offline models (Nelson (2000), (Carlson et al. 2007) and NFDRS) forced by WRF weather output.

DFM and ERC are calculated from meteorological variables predicted using WRF version 3.5 (Skamarock et al. 2008), run at 3 km and 6 km horizontal resolution. We selected a WRF configuration which minimized errors with respect to near-surface temperature, winds, and dew point during Santa Ana Wind events (Cao 2015; Cao and Fovell 2016). This configuration includes

the simple WRF Single-Moment 3-class microphysics scheme (Hong et al. 2004), RRTMG shortwave and longwave radiation schemes (Iacono et al. 2008), the MM5 Monin-Obukhov surface layer scheme, and the Asymmetrical Convective Model version 2 boundary layer scheme (Pleim 2007). The Noah land-surface model (Tewari et al. 2004) with 4 soil layers was used in conjunction with the MODIS land use dataset. Each operational WRF forecast dynamically downscales the 12 km resolution 00Z and 12Z North American Mesoscale Forecast System (NAM) 1-3.5 day forecasts to 3 km resolution. We use a two-way nested WRF domain configuration consisting of a 3 km resolution innermost domain nested within a 9 km resolution outermost domain with 51 vertical levels. To extend the forecast out to 6 days, the 0.25° resolution Global Forecast System (GFS) is downscaled using WRF to 6 km resolution. We use a two-way nested WRF domain configuration consisting of a 6 km resolution innermost domain nested within an 18 km outer and 54 km outermost domain with 46 vertical levels. To help determine bounds and behavior of the SAWTI equations and place forecasts in historical perspective, we dynamically-downscaled the 32 km resolution North American Regional Reanalysis (NARR, (Mesinger et al. 2006)) data set to 3 km resolution using WRF over the historical period spanning January 1984 through December 2013. We used a two-way nested WRF domain configuration consisting of a 27 km resolution outer, 9 km resolution inner and 3 km resolution innermost domain with 51 vertical levels. WRF was integrated across 3.5 day periods with the first 12 hours from each period discarded as spin-up time.

b. Calculating SAWTI

1) WEATHER

Equation 1 is temporally averaged at each WRF grid point across the domain using the following equation:

$$\mathrm{LFP_{w,gpx}} = \frac{\mathrm{LFP_{w}}hour1 + \mathrm{LFP_{w}}hour2 + ... + \mathrm{LFP_{w}}hour8}{8} \tag{7}$$

where $\mathrm{LFP_{w,gpx}}$ is an average $\mathrm{LFP_{w}}$ value over an eight-hour time period at grid point x. An eight hour time period was chosen because that is ample time for the finer fuels (i.e., $\mathrm{DFM_{10hr}}$) to respond to the ambient atmospheric conditions. Once an average $\mathrm{LFP_{w}}$ had been calculated for each grid point, the maximum eight hour average $\mathrm{LFP_{w}}$ for each day is then spatially averaged over each zone as follows:

$$\mathrm{LFP_{w,zone}} = \frac{\mathrm{LFP_{w}}gp1 + \mathrm{LFP_{w}}gp2 + ... + \mathrm{LFP_{w}}gpx}{Number\ of\ grid\ points\ per\ zone} \tag{8}$$

where $\mathrm{LFP_{w,zone}}$ is the maximum 8 hr averages at each grid point within the model domain. It is important to note that (7) was calculated for five different eight consecutive hour time periods with the highest value chosen to represent each zone for the day (Figure 10). This is to ensure that the worst conditions are being captured on a daily basis. For instance while most Santa Ana wind events peak during the morning hours, some events can peak later in the day or at night depending on the arrival time of stronger dynamical support. Thus calculating $\mathrm{LFP_{w}}$ for only one consecutive eight-hour time period may fail to capture the worst conditions of the day. This more simplistic approach was favored compared to using an 8 hr running average.

2) FUELS

Recall that DL relates ERC and DFM to historical fire activity. To provide a DL forecast, DFM and ERC are computed across the spun-up WRF forecast period. To avoid the potentially

long spin-up times required by DFM, the DFM must be initialized at each grid point across the WRF domain. Since a publicly-available gridded observed DFM product does not exist, DFM is initialized using the previous day's DFM forecast valid at the 4^{th} hour of the current WRF forecast. The first four hours of each WRF forecast are removed to allow for model spin-up and avoid contamination of DFM and ERC due to relatively unrealistic atmospheric inputs. Due to the need for this continuous spun-up DFM time series, WRF forecasts must be uninterrupted. However, if any WRF forecasts are missed, DFM forecasts could be initialized using output from earlier WRF/DFM forecasts which are archived for at least a month.

Quasi-observational data (NLDAS–2) is available for estimating LFM and NDVI using equations 3 and 5, respectively. The 22-day lagged soil moisture required for LFM is provided from the Noah land surface model output of the NLDAS–2 dataset. For NDVI, the latest NLDAS–2 output is used (typically a five day lag) which provides vegetation fraction, 2 m relative humidity, and soil moisture. Archived NLDAS–2 data is needed going back to the previous September 1 for cumulative precipitation. Both LFM and NDVI are re-gridded from the NLDAS–2 12.5 km to the 3 km horizontal resolution matching the WRF domain using bilinear interpolation and held constant across the 6-day forecast period. In contrast to weather which is calculated hourly, fuel conditions are calculated only at 1300 LST, representing fuel conditions for the entire day.

c. Public Dissemination

Social science was incorporated during the early stages of the developmental process of SAWTI (Wall, et al. 2014). The Desert Research Institute provided a social scientist to conduct an in-depth survey of 5 communities across Southern California. Much of the survey centered on questions regarding how the public obtains weather and fire information, and their associated responses to that information. The results of the survey were used to help determine the type of information

that would be presented in the product. In conjunction with the social science, historical weather and fuels data were correlated to historical fire occurrence records to develop index threat level categories. For example, for each SAWTI zone we compared daily FMC values along with daily LFP_w values from (1) for the historical period (1992–2011) to whether or not a fire had occurred. We repeated the process this time equating the output to whether or not a 100 hectare fire or greater occurred (Figure 11). Comparing these two results yielded a conditional probability for an ignition to reach or exceed 100 hectares based on FMC and LFP values. By assessing and employing these probabilities, LFP breakpoints could easily be determined (see section e for more details).

The SAWTI has 4 threat levels that range from "Marginal" to "Extreme". When Santa Ana winds are either not expected or will not contribute to significant fire activity, then a "No Rating" is issued for that day. For example, it could be possible that if a strong Santa Ana wind event were to transpire after appreciable rains occurred or when fuels are wet, the event would be categorized as a "No Rating". For definitions of other threat levels, see Table 3. Tied to each threat level is a list of recommended actions suggested to the public to better prepare for an impending event. Examples include: "Clean debris away from your house, charge your cell phone and make sure you have plenty of gas". The list of recommended actions expands as the threat levels increase. This aspect of the product is critical as it serves to link categories of severity with public awareness.

The product consists of an online webpage (`http://sawti.fs.fed.us`) that displays a 6-day forecast of the above mentioned categories for each of the 4 zones across Southern California (Figure 12). A map of the region stands as the centerpiece of the page and graphically shows the categories which are colorized ranging from grey ("No Rating") to purple ("Extreme"). The product is issued once daily but can be updated more frequently if conditions warrant. The webpage allows users to obtain more information such as viewing the latest weather observation from select stations when zoomed in on the map. The page will also display active and non-active fires (via

icons) on the map when such activity is present. Selecting one of these icons will provide the user with specific fire information such as acreage burned, percent contained, and links to more data. SAWTI also has a Twitter feed (`https://twitter.com/sawti_forecast`) where users are notified about changes in threat levels.

The product was beta tested for a year prior to it becoming a public product in the fall of 2014. During the beta test phase, the index performed well in capturing all events that occurred during the fall of 2013 through the spring of 2014 which ranged from "No Rating" to "High". Several notable events include: 16 January 2014 (Colby fire), 29 April 2014-1 May 2014 (Etiwanda fire), and 13-14 May 2014 (the San Diego fires). Fire agencies that were granted access to the index during this time used the product to make critical decisions regarding the allocation and mobilization of shared fire resources prior to when these fires occurred. Specifically, the event that occurred on 13-14 May 2014 was especially notable due to the fact that winds were unusually strong during this period, and that multiple large fires occurred as a result. Figure 13 shows a map of the fires across San Diego County, while Figure 14 shows the SAWTI in beta test form for this event. The product was officially released to the public on September 17, 2014 via a press release and an associated press conference. Since that time, the product has been used by local news media across the San Diego and Los Angeles metropolitan areas, as well as being shown on The Weather Channel.

d. Validation

Fire potential is very difficult to validate since our model is based on a conditional probability (i.e., getting an ignition). In addition, once an ignition occurs there are a number of human behaviors that cannot be predicted which can influence fire potential. For instance, if the SAWTI indicates a high likelihood of having a large fire for a particular Santa Ana wind event and one does not occur, it does not necessarily mean the model performed poorly. There may not have

been an ignition during the event, or there may have been an ignition, but adequate fire-fighting resources were made available to be successful in suppressing the incident before becoming large. There have been a few times where the index displayed a "No Rating" and a large fire occurred, but this is very rare.

Modeling fuel conditions accurately presents certain challenges. Regarding DFM, validating WRF DFM and ERC is limited given the sparse observations across this domain. Various Remote Automated Weather Stations (RAWS) calculate DFM using measured atmospheric inputs including near-surface temperature, relative humidity, precipitation, and solar radiation. We validate WRF DFM and ERC across 2 years of the 30 year historical period at 14 RAWS (Figure 15). These stations were selected so that at least 3 stations represent zones 1, 2 and 3. Zone 4 has relatively fewer RAWS reporting DFM and ERC measurements for the time period of interest, thus only 1 station represents zone 4. At each RAWS location, the closest WRF gridcell with the smallest elevation difference was selected for validation. We show 2 example timeseries plots (Figures 16 and 17) for Goose Valley and Claremont RAWS. At the Goose Valley RAWS site (Figure 16), WRF DFM and ERC output agrees well with RAWS measurements for most of the 2 years examined with only a slightly positive bias of 0.24 and 2.14 for $\mathrm{DFM}_{100\mathrm{hr}}$ and $\mathrm{DFM}_{1000\mathrm{hr}}$, respectively. At the Claremont RAWS (Figure 17), WRF DFM and ERC output compares less favorably at certain times over the 2 years and strongly during others. However, we report small biases at the Claremont RAWS of -1.27 and 1.30 for $\mathrm{DFM}_{100\mathrm{hr}}$ and $\mathrm{DFM}_{1000\mathrm{hr}}$, respectively, with RMSEs of 4.22 and 2.65. Table 4 shows WRF error statistics for all 14 RAWS across the 2 year period. The WRF $\mathrm{DFM}_{100\mathrm{hr}}$ bias ranges from -1.27 to 4.00, RMSE ranges from 2.72 to 4.93 with correlation ranging from 0.55 to 0.86. Our WRF $\mathrm{DFM}_{1000\mathrm{hr}}$ has a positive bias ranging from 1.30 to 6.00, RMSE spanning 2.50 to 6.15 and correlation from 0.54 to 0.92. Finally, WRF ERC bias is mostly negative given the positive $\mathrm{DFM}_{1000\mathrm{hr}}$ bias ranging from -25.09 to 0.50, RMSE

ranging from 9.52 to 27.41 and correlation from 0.53 to 0.90. It is hypothesized that WRF does not adequately resolve the complex topography at the two RAWS that have the worst error statistics, Chilao and Palomar.

e. Climatology

The historical dataset described previously provides us with an unprecedented 30 year climatology of the fuel and weather variables related to wildfires across the 4 SAWTI zones in Southern California. Having this dataset has allowed us first to create breakpoints within the raw SAWTI output necessary for the development of the 4 threat levels which are integral to the final public product. To do this, we correlated historical fire occurrence data with historical LFP_w values from the dataset to develop breakpoints for the SAWTI. Most of the breakpoints fell naturally but with some minor adjustments we created breakpoints at the 50^{th}, 75^{th}, 90^{th}, and 97^{th} percentiles. Significant increases in conditional probabilities for each category seemed to confirm our choices.

This unique dataset informs us about the historical significance the fuels, weather, and SAWTI events have had during the past 30 years. Having the ability to put past, but perhaps more importantly, forecasted SAWTI events into historical perspective helps inform the public and first responders about the nature and the characteristic of an impending event. For example, we can authoritatively state that the Santa Ana wind event which helped to spawn the Witch Creek Fire (and served as the catalyst for the development of this index) was ranked the highest event in the 30 year dataset for zones 1 and 2.

As we continue to explore this dataset, we hope to gain a better understanding of the climatology of Santa Ana winds during the past 3 decades, including detecting and understanding inter-annual trends and cycles in event frequencies and strength. Figure 18 shows the number of days when Santa Ana winds occurred across zone 3 for the period spanning 1984 to 2013. This figure reveals

a noticeable upward trend in the frequency of Santa Ana wind days during approximately the last 10 years ending in 2013. Preliminary research shows that this long-term trend in frequency (possibly associated with a longer-term inter-annual cycle) coincides with a predominately negative phase of the Pacific Decadal Oscillation (PDO). Further investigation conducted in a future paper will seek to explore the causal mechanisms for this trend in frequency, as well as other trends in Santa Ana wind characteristics.

4. Summary and Conclusions

As the Wildland Urban Interface (WUI) continues to expand across Southern California, the source of ignitions will increase leading to a greater probability for large and destructive fires during Santa Ana wind events. This puts the public and firefighter safety at risk, thus the increasing need to categorize such events in terms of their effect on the fire environment.

Predictive Services' initial efforts to categorize Sana Ana winds helped to provide the leadership and guidance necessary for the development of the SAWTI. Through the successful collaboration between government, academia, and the private sector, high resolution model data along with satellite derived variables allowed us to incorporate fuel and weather data into the index on a gridded domain within Southern California. Challenges surrounding the assessment of fuel conditions include the difficulty in determining different fuel moisture parameters which can sometimes result in a less accurate evaluation of fuel conditions. Further refinement of the model is needed to improve the overall output. However, during the beta test process, the index performed very well with positive responses from the recipients of the preliminary output. Since its public unveiling, the index has been well received by the media and the fire community.

Our 30 year dataset is unprecedented. Not only does it provide us with 30 years of fuel moisture data across southern California (which is useful in relating fuel conditions with drought), it also

gives us quantifiable outputs of average wind velocity, dew point depression, and the SAWTI itself. This allows us to put past and future Santa Ana events (magnitude, duration, and spatial coverage) into historical perspective which is significant. Future studies in the climatology of such events can be conducted leading to a better understanding of why certain trends exist.

Fire agencies and first responders, private industry, the general public, and the media now have a new operational tool that determines the severity of Santa Ana wind events. Furthermore, they will have a clearer understanding of the severity of an event based on the potential for large fires to occur. Specifically, a more effective media response will result in the general population (particularly those living within the WUI) being more proactive in its response to an impending event.

Acknowledgments. The authors would like to thank Dr. Jim Means for his helpful suggestions and input into this project. We also appreciate the advice from Beth Hall, Tamara Wall, Mark Jackson, and Alex Tardy. The data used in this study were acquired as part of the mission of NASA's Earth Science Division and archived and distributed by the Goddard Earth Sciences (GES) Data and Information Services Center (DISC). Major funding for this project was provided by SDG&E.

References

Blier, W., 1998: The Sundowner Winds of Santa Barbara, California. *Wea. Forecasting*, **13**, 702–716, doi:http://dx.doi.org/10.1175/1520-0434(1998)013⟨0702:TSWOSB⟩2.0.CO;2.

Bradshaw, L. S., R. E. Burgan, J. D. Cohen, and J. E. Deeming, 1983: The 1978 national fire danger rating system: Technical documentation. *General Technical Report INT-169*.

Cao, Y., 2015: The santa ana winds of southern california in the context of fire weather. Ph.D. thesis, The University of California, Los Angeles, 172 pp.

503 Cao, Y., and Fovell, R. G., 2016: Downslope Windstorms of San Diego County. Part I: A Case
504 Study. *Mon. Wea. Rev.*, **144**, 529–552, doi:10.1175/MWR-D-15-0147.1.

505 Carlson, J. D., Bradshaw, L. S., R. M. Nelson Jr., R. R. Bensch and R. Jabrzemski, 2007: Applica-
506 tion of the Nelson model to four timelag fuel classes using Oklahoma field observations: model
507 evaluation and comparison with National Fire Danger Rating System algorithms. *International*
508 *Journal of Wildland Fire*, **16**, 204–216.

509 Castro, F. X., A. Tudela, and M. Sebastiá, 2003: Modeling moisture content in shrubs to predict
510 fire risk in catalonia (spain). *Agricultural and Forest Meteorology*, **116**, 49–59, doi:10.1016/
511 S0168-1923(02)00248-4.

512 Chuvieco, E., D. Cocero, D. Riaño, P. Martin, J. Martínez-Vega, J. de la Riva, and F. Pérez, 2004:
513 Combining ndvi and surface temperature for the estimation of live fuel moisture content in forest
514 fire danger rating. *Remote Sensing of Environment*, **92**, 322–331, doi:10.1016/j.rse.2004.01.019.

515 Clinton, N. E., C. Potter, B. Crabtree, V. Genovese, P. Gross, and P. Gong, 2010: Remote sensing-
516 based time-series analysis of cheatgrass (bromus tectorum l.) phenology. *J. Environ. Qual.*, **39**,
517 955–963, doi:10.2134/jeq2009.0158.

518 Countryman, C. M., and C. W. Philpot, 1970: Physical characteristics of chamise as a wild-
519 land fuel. *Research Paper PSW-66*, [Available online at http://www.fs.fed.us/psw/publications/
520 documents/psw_rp066/psw_rp066.pdf].

521 Elmore, A. J., J. F. Mustard, S. J. Manning, and D. B. Lobell, 2000: Quantifying vegetation
522 change in semiarid environments: Precision and accuracy of spectral mixture analysis and the
523 normalized difference vegetation index. *Remote Sens. of Environ.*, **73**, 87–102.

524 Fosberg, M. A., 1978: Weather in wildland fire management: the fire weather index. *Conference*
525 *on Sierra Nevada Meteorology*, pp. 1–4, June 19–21 Lake Tahoe, CA.

526 Fovell, R. G., 2012: Downslope Windstorms of San Diego County; Sensitivity to Resolution and
527 Model Physics. *13th WRF Users Workshop*.

528 Fovell, R. G., T. Rolinski, Y. Cao, and D. Weise, 2016: A simple model for the live fuel moisture
529 of chamise. Submitted to *Int. J. Wildland Fire*.

530 Hong, S.-Y., J. Dudhia, and S.-H. Chen, 2004: A revised approach to ice microphysical processes
531 for the bulk parameterization of clouds and precipitation. *Mon. Wea. Rev.*, **132**, 103–120.

532 Hughes, M., and A. Hall, 2010: Local and Synoptic Mechanisms Causing Southern California's
533 Santa Ana Winds. *Clim. Dyn.*, **34(6)**, 847–857, doi:10.1007/s00382-009-0650-4.

534 Iacono, M. J., J. S. Delamere, E. J. Mlawer, M. W. Shephard, S. A. Clough, and W. D. Collins,
535 2008: Radiative forcing by long-lived greenhouse gases: Calculations with the AER radiative
536 transfer models. *J. Geophys. Res.*, **113**, D13 103, doi:10.1029/2008JD009944.

537 Jin, Y., Goulden, M. L., Faivre, N., Veraverbeke, S., Sun, F., Hall, A., Hand, M., Hook, S. and
538 Randerson, J. T., 2015: Identification of two distinct fire regimes in Southern California: im-
539 plications for economic impact and future change. *Environ. Res. Lett.* **10** (2015)094005, doi:
540 10.1088/1748-9326/10/9/094005

541 Mesinger, F., DiMego, G., Kalnay, E., Mitchell, K., Shafran, P., Ebisuzaki, W., Jovic, D., Woollen,
542 J., Rogers, E., Berbery, E., Ek, M. B., Fan, Y., Grumbine, R., Higgins, W., Li, H., Lin, Y.,
543 Manikin, G., Parrish, D., and Shi, W., 2006: NORTH AMERICAN REGIONAL REANALY-
544 SIS. *Bull. Am. Meteorol. Soc.*, **87(3)**, 343–360, doi:10.1175/BAMS-87-3-343.

Moritz, M. A., T. J. Moody, M. A. Krawchuck, M. Hughes, and A. Hall, 2010: Spatial variation in extreme winds predicts large wildfire location in chaparral ecosystems. *Geophys. Res. Lett.*, **37**, 1–5, doi:10.1029/2009GL041735.

Nelson, R. M., 2000: Prediction of diurnal change in 10-h fuel stick moisture content. *Canadian Journal of Forest Research*, **30(7)**, 1071–1087, doi:10.1139/x00-032.

Pleim, J. E., 2007: A combined local and nonlocal closure model for the atmospheric boundary layer part I: Model description and testing. *J. Appl. Meteor.*, **46**, 1383–1395, doi:10.1175/JAM2539.1.

Pollet, J., and A. Brown, 2007: Fuel moisture sampling guide. Salt Lake City, UT: U.S. Department of the Interior, Bureau of Land Management, Utah State Office, 32 p..

Preisler, H. K., S. C. Chen, F. Fujioka, J. W. Benoit, and A. L. Westerling, 2008: Wildland fire probabilities estimated from weather model-deduced monthly mean fire danger indices. *International Journal of Wildland fires*, **17(3)**, 305–316, doi:10.1071/WF06162.

Raphael, M. N., 2003: The Santa Ana Winds of California. *Earth Interactions*, **7**, 1–13, doi:10.1175/1087-3562(2003)007⟨0001:TSAWOC⟩2.0.CO;2.

Rolinski, T., D. Eichhorn, B. J. D'Agostino, S. Vanderburg, and J. D. Means, 2011: Santa Ana Forecasting and Classification. *American Geophysical Union, Fall Meeting*, **abstract #NH33B-1573**.

Rothermel, R. C., 1972: A mathematical model for predicting fire spread in wildland fuels. *Research Paper INT-115*.

Skamarock, W. C., and Coauthors, 2008: A description of the advanced reasearch WRF version 3. *NCAR Technical Note*, **NCAR/TN-475+STR**.

Tewari, M., and Coauthors, 2004: Implementation and verification of the unified noah land surface model in the WRF model. 20^{th} *conference on weather analysis and forecasting/16th conference on numerial weather prediction*, 11–15.

Wall, T. U., A.L. Knox Velez, and J. Diaz. 2014. Wildfire Readiness in the Southern California Wildland-Urban Interface: Understanding Wildfire Preparedness and Evacuation Readiness Among Residents in Southern Californias Wildland-urban Interface. Research report produced by the Desert Research Institute. [Available online at: http://www.dri.edu/publications/dripublications].

White, M. A., P. E. Thornton, and S. W. Running, 1997: A continental phenology model for monitoring vegetation responses to inter-annual climatic variability. *Global Biogeochem. Cycles*, **11**, 217–234, doi:10.1029/97GB00330.

LIST OF TABLES

TABLE 1: Relationship between NDVI and greenness.

NDVI	G_{ag} *Number*	*Description*
$NDVI > 0.64$	0	Green
$0.59 < \text{NDVI} \leq 0.64$	1	
$0.54 < \text{NDVI} \leq 0.59$	2	
$0.49 < \text{NDVI} \leq 0.54$	3	
$0.39 < \text{NDVI} \leq 0.49$	4	
$0 \leq \text{NDVI} \leq 0.39$	5	Cured

TABLE 2: Selected NDVI Regressors.

Coefficient	*Value*
α	-0.314867
β_1	0.11253592
β_2	1.44E-05
β_3	0.00355647
β_4	0.911360168
β_5	0.002412815

TABLE 3: Categories of threat levels and their descriptions.

Category	*Description*
NO RATING	Santa Ana winds are either not expected, ***or*** will not contribute to significant fire activity.
MARGINAL	Upon ignition, fires ***may*** grow rapidly.
MODERATE	Upon ignition, fires ***will*** grow rapidly and ***will*** be difficult to control.
HIGH	Upon ignition, fires will grow ***very*** rapidly, will burn intensely, and will be ***very*** difficult to control.
EXTREME	Upon ignition, fires will have extreme growth, will burn ***very*** intensely, and will be uncontrollable.

TABLE 4: WRF error statistics at each RAWS for time spanning January 2012 through December 2013.

	100hr DFM			1000hr DFM			ERC		
Station Name	*Bias*	*RMSE*	*CORR*	*Bias*	*RMSE*	*CORR*	*Bias*	*RMSE*	*CORR*
Camp Elliot	0.17	3.90	0.55	1.75	2.97	0.54	−0.71	11.12	0.53
Cheeseboro	0.99	3.30	0.69	3.89	4.25	0.75	−10.78	14.81	0.74
Chilao	4.00	4.93	0.84	6.00	6.15	0.92	−25.09	27.41	0.89
Claremont	−1.27	4.22	0.66	1.30	2.65	0.76	0.50	13.71	0.79
Clark	−0.06	3.24	0.69	2.80	3.39	0.75	−4.27	11.24	0.76
Descanso	2.45	4.07	0.82	3.93	4.40	0.85	−14.40	18.39	0.84
El Cariso	1.26	3.70	0.73	3.27	3.94	0.81	−9.19	15.02	0.82
Fremont Canyon	−0.03	3.73	0.66	2.21	3.13	0.63	−2.52	11.25	0.73
Goose Valley	0.24	3.96	0.65	2.14	2.90	0.78	−4.82	11.50	0.77
Julian	0.95	3.97	0.80	2.36	3.05	0.90	−4.81	10.54	0.90
Los Prietos	−0.97	2.72	0.74	1.69	2.67	0.72	−3.27	10.45	0.72
Palomar	3.06	4.46	0.86	4.12	4.82	0.88	−14.72	20.12	0.88
Rose Valley	0.74	2.83	0.77	3.06	3.45	0.85	−10.06	14.06	0.82
Valley Center	−0.22	3.80	0.67	1.84	2.50	0.80	−2.32	9.52	0.78

LIST OF FIGURES

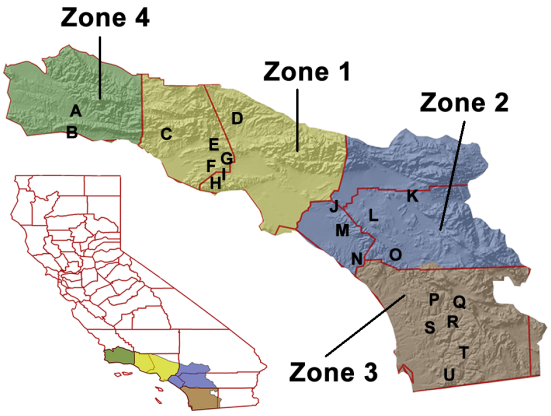

Location	Site
A	Santa Ynez Valley
B	Refugio State Beach
C	Ojai
D	Castaic Lake
E	Middle Range Fire Rd
F	Oakbrook
G	Simi Valley
H	Upper Las Virgenes
I	Cheeseboro
J	Chino Hills State Park
K	San Timoteo Canyon
L	Lake Mathews
M	Silverado Canyon
N	San Juan Capistrano
O	Santa Rosa Plateau
P	Guejito
Q	Mesa Grande
R	Witch Creek
S	Highland Valley Rd
T	Viejas
U	Honey Springs Rd

FIG. 1: Map of SAWTI zones. Inset shows SAWTI zones in reference to the state of California. Letters denote location of NDVI grassland sites with underlying topography shaded. Site names are provided in the lookup table to the right. County boundaries shown in red.

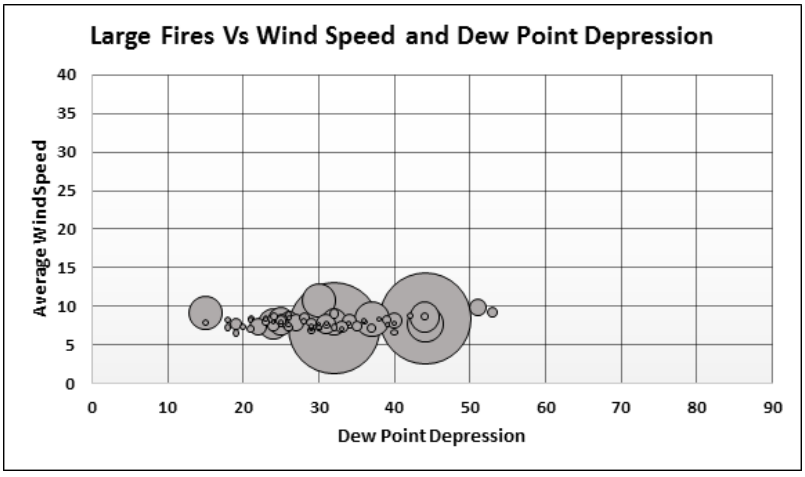

FIG. 2: Relationship of large fire ($\geq$ 100 hectares) occurrence and relative size with respect to average wind speed and dew point depression across zone 1 between June 1st and September 20th from 1992 to 2012. Bubble size represents relative fire size.

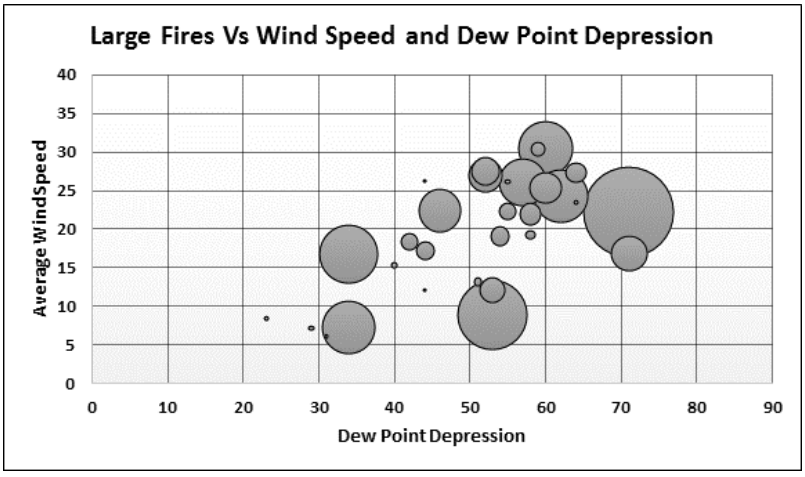

FIG. 3: Same as Figure 2 except between September 21st through December 31st.

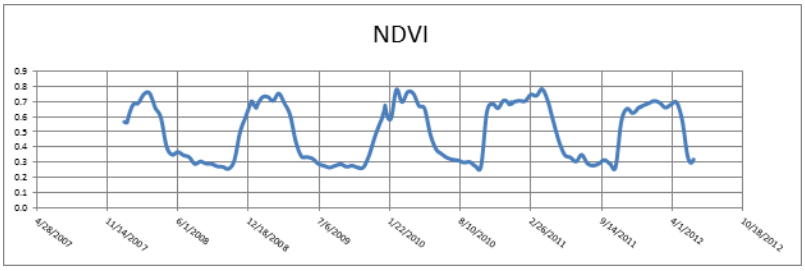

FIG. 4: Sample annual NDVI output.

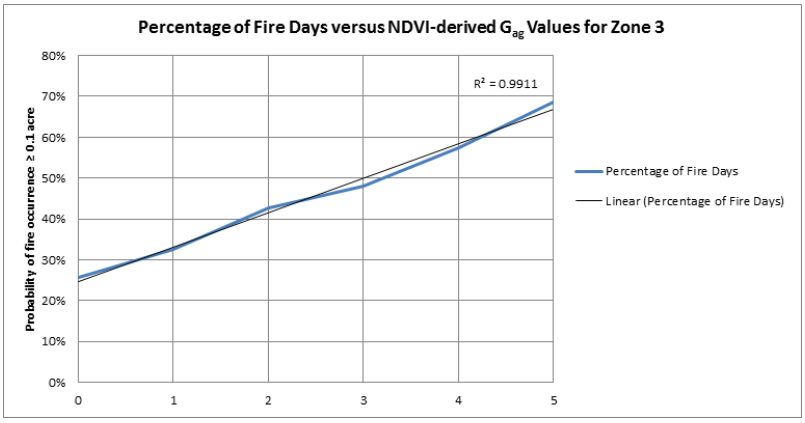

FIG. 5: Probability of fires ≥ 0.04 hectares predicted by NDVI-derived G_{ag} for zone 3.

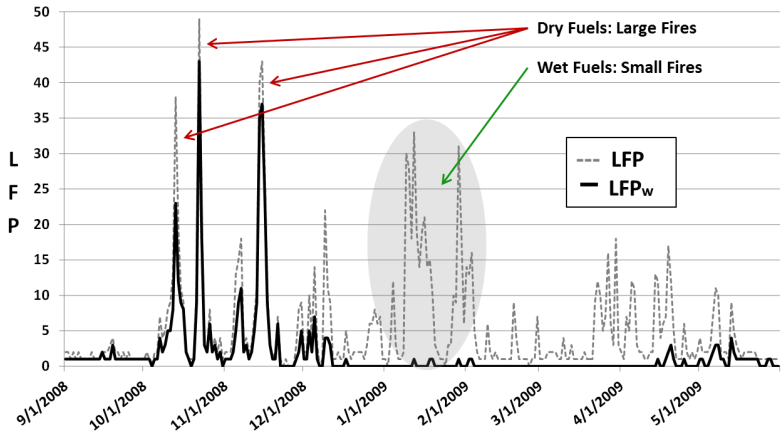

FIG. 6: Comparison of LFP_w and LFP timeseries for zone 1 during the period spanning September 2008 through May 2009. For large fires that occurred in October and November of 2008, relatively dry fuels (LFP, solid black line) accompanied the dry and windy weather (LFP_w, dashed grey line). In contrast, January through February of 2009, experienced peaks of windy and dry conditions (LFP_w) accompanied by moist fuels (LFP) and, as a result, no fires grew larger than 100 hectares.

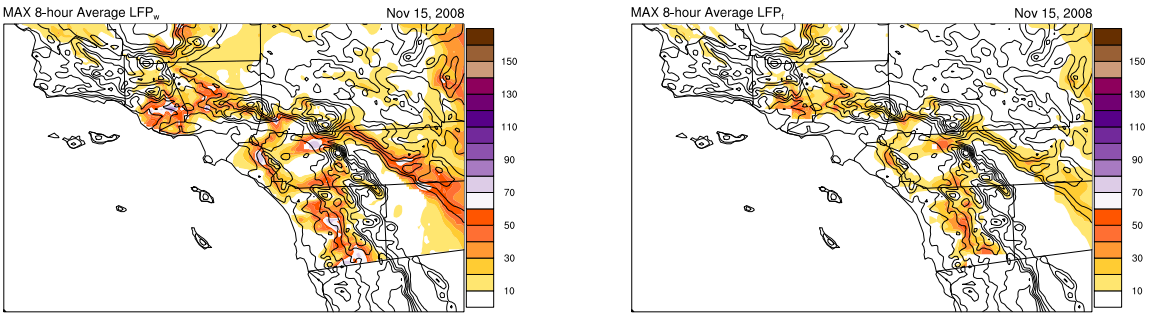

FIG. 7: Average LFP_W (left) and LFP (right) from 8am to 3pm during a Santa Ana event on November 15, 2008. This offshore event was accompanied by the Freeway Complex Fire which burned over $12,141$ hectares while destroying 187 homes and damaging 117 others (http://cdfdata.fire.ca.gov/incidents/incidents_details_info?incident_id=305).

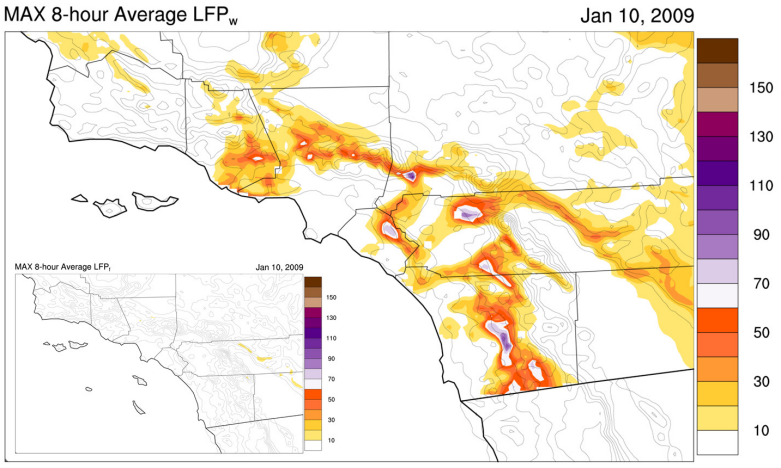

FIG. 8: Average LFP_w (large) and LFP (lower left) from 8am to 3pm during a Santa Ana event on January 2009.

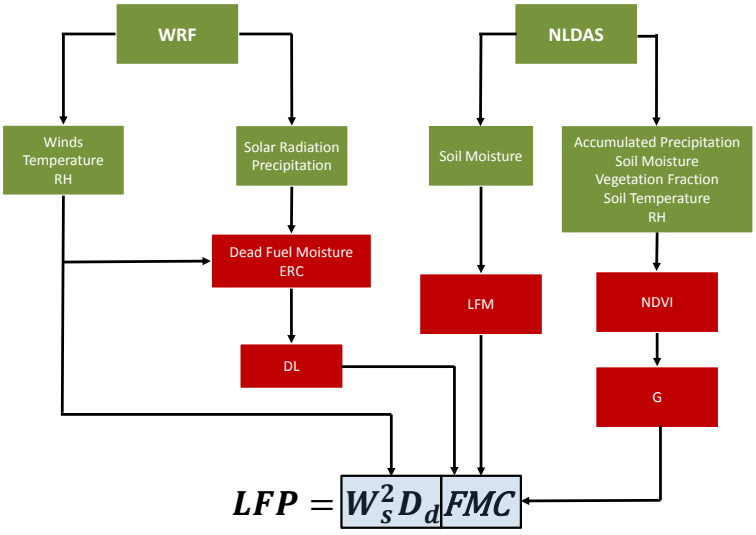

FIG. 9: Flowchart depicting operational LFP input models and datasets, derived variables and final LFP equation.

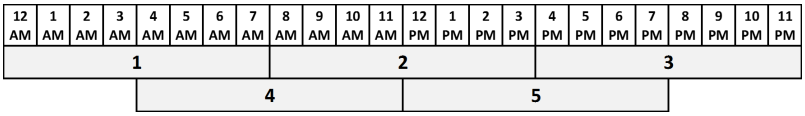

FIG. 10: Time periods over which LFP_w is averaged.

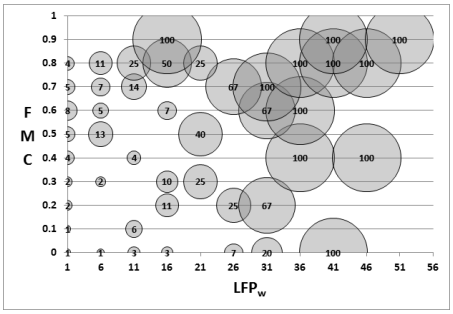

FIG. 11: Using historical fire occurrence data between 1992–2011, we show the relationship between binned FMC, LFP_w and fire activity for zone 1. Tickmarks indicate starting bin values for both FMC (bin interval of 0.099) and LFP_w(bin interval of 5). Bubble size indicates the conditional probability for an ignition to meet or exceed 100 hectares. For instance, 100% of fires which ignited during conditions characterized with FMC ≥ 0.7 and $LFP_w \geq 36$ grew into large fires.

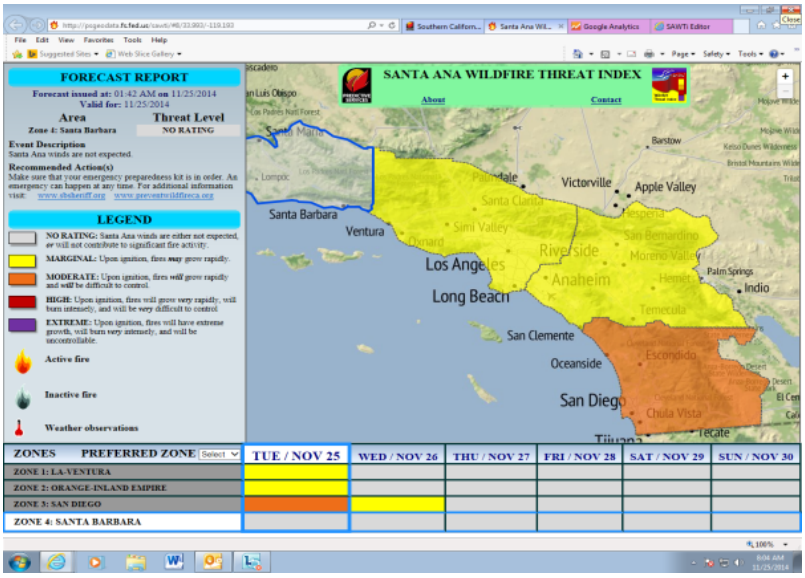

FIG. 12: Online operational SAWTI product.

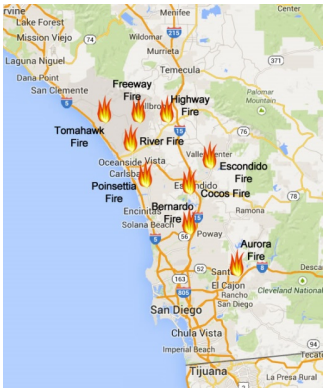

FIG. 13: Map of active fires (icons) on May 14, 2014 across San Diego County.

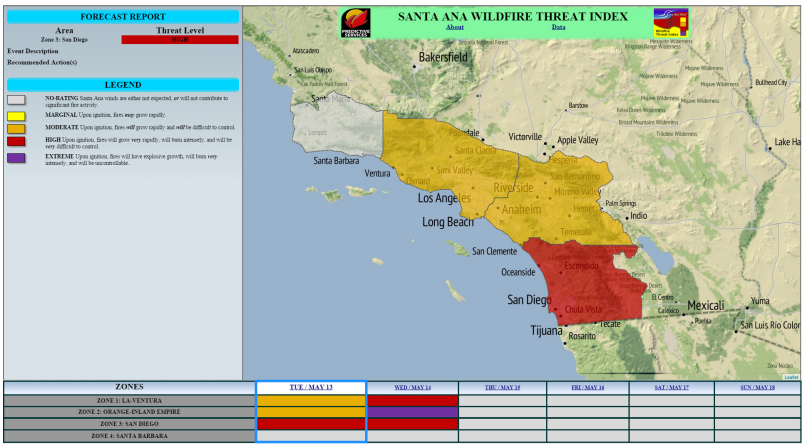

FIG. 14: SAWTI (in beta test) during May 14-15, 2014.

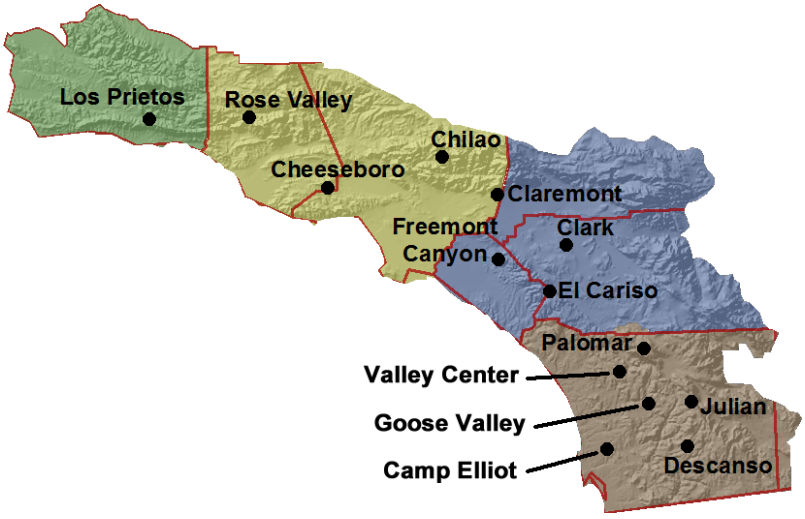

FIG. 15: RAWS used to validate WRF DFM and ERC.

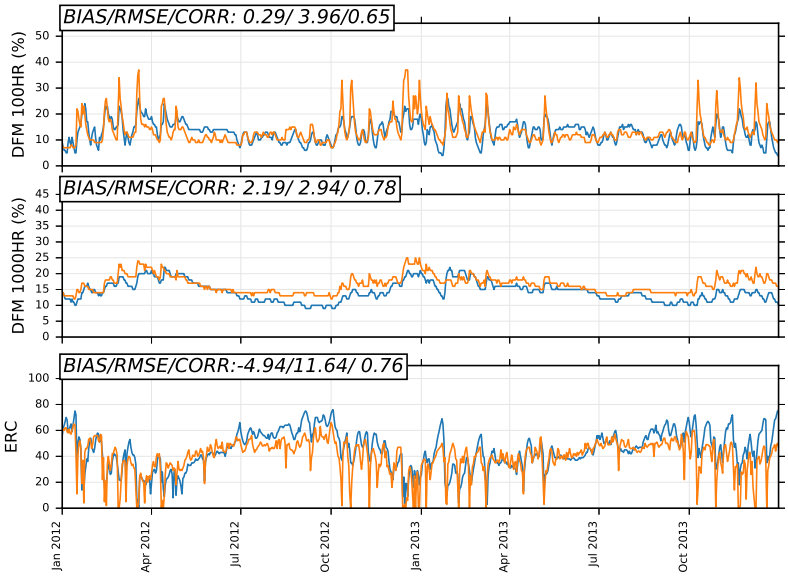

FIG. 16: RAWS (blue line) and closest WRF gridcell (orange line) timeseries of 100 (top) and 1000 hr (middle) dead fuel moisture and ERC (bottom row) spanning January 2012 through December 2013 for Goose Valley. WRF output coincides with RAWS 1300 LST measurements. Each plot is annotated with WRF output bias, RMSE and Spearman correlation.

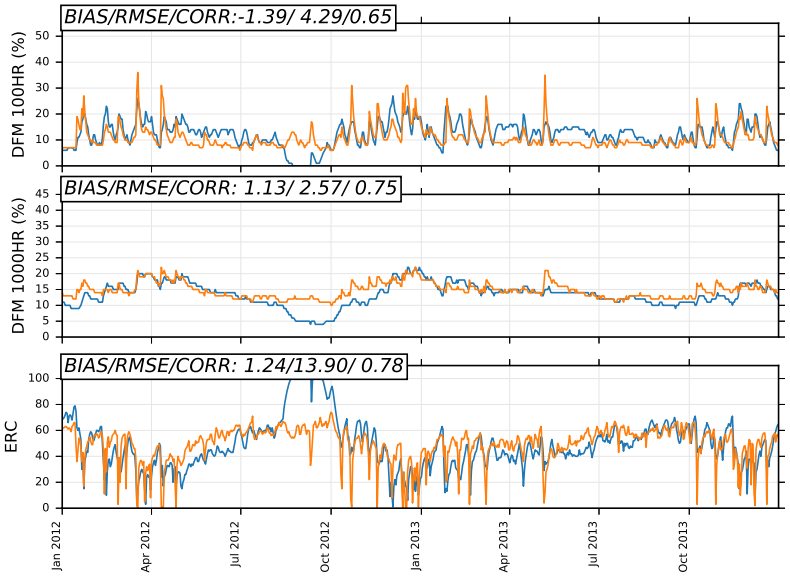

FIG. 17: Same as figure 16 except for Claremont RAWS.

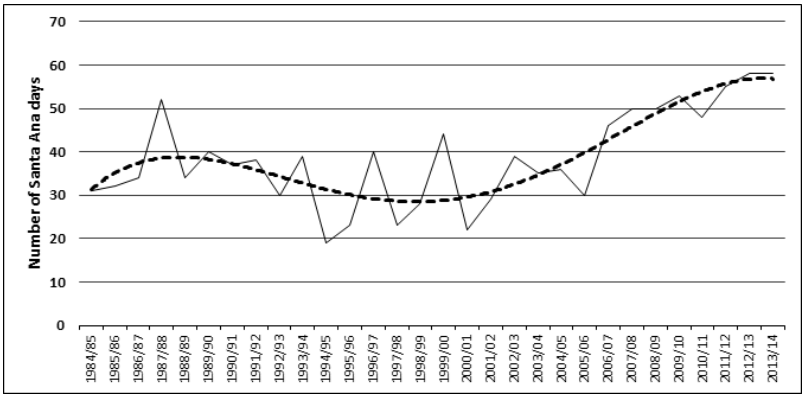

FIG. 18: Number of Santa Ana wind days per rain year (July 1 through June 30) for years spanning 1984–2014 (solid black line). Dashed line is a polynomial fit to the data which helps depict the longer-time period trends.

Attachment: Downslope Windstorms of San Diego County. Part I: A Case Study (Cao & Fovell)

Downslope Windstorms of San Diego County. Part I: A Case Study

YANG CAO AND ROBERT G. FOVELL

Department of Atmospheric and Oceanic Sciences, University of California, Los Angeles, Los Angeles, California

(Manuscript received 9 April 2015, in final form 27 October 2015)

ABSTRACT

The "Santa Ana" wind is an offshore flow that affects Southern California periodically during the winter half of the year, typically between September and May. The winds can be locally gusty, particularly in the complex terrain of San Diego County, where the winds have characteristics of downslope windstorms. These winds can cause and/or rapidly spread wildfires, the threat of which is particularly acute during the autumn season before the onset of winter rains. San Diego's largest fires, including the Cedar fire of 2003 and Witch Creek fire of 2007, occurred during Santa Ana wind events.

A case study of downslope flow during a moderately intense Santa Ana event during mid-February 2013 is presented. Motivated by the need to forecast winds impinging on electrical lines, the authors make use of an exceptionally dense network of near-surface observations in San Diego County to calibrate and verify simulations made utilizing the Advanced Research version of the Weather Research and Forecasting (WRF) Model, which in turn is employed to augment the observations. Results demonstrate that this particular Santa Ana episode consists of two pulses separated by a protracted lull. During the first pulse, the downslope flow is characterized by a prominent hydraulic jumplike feature, while during the second one the flow possesses a clear temporal progression of winds downslope. WRF has skill in capturing the evolution and magnitude of the event at most locations, although most model configurations overpredict the observed sustained wind and the forecast bias is itself biased.

1. Introduction

Southern California is known for its "Santa Ana" winds, which were named after a city and canyon in Orange County, California. The Santa Anas are very dry, sometimes hot, offshore winds directed from the Great Basin and Mojave Desert over the mountains and through the passes of Southern California (cf. Sommers 1978; Small 1995) that can produce gusts exceeding 45 m s^{-1} (100 mph) in favored areas.[1] The winds evince terrain-associated amplification of the mountain gap and downslope varieties (Huang et al. 2009; Hughes and Hall 2010). Santa Ana events occur most frequently between October and February, with December being the peak month (Raphael 2003; Jones et al. 2010). Its season is often thought of as extending from September to April, although recent years (2013 and 2014) have seen events of significant strength during the month of May.

Although the Santa Anas tend to form most frequently in midwinter, the most dangerous events often occur in autumn, before the winter rains have begun (Sommers 1978; Westerling et al. 2004). At that time, the vegetation tends to be extremely dry, and fire danger is elevated owing to the combination of low to very low humidity and strong winds that can spark and spread flames. Autumn fires historically have the potential to be very large in area, being fanned by the Santa Ana winds (Chang and Schoenberg 2011).

Santa Ana events result when cooler air spills across the Great Basin, becoming partially dammed by the mountains that separate Southern California from the inland deserts. This increases the horizontal gradient in sea level pressure (SLP) and helps to enhance flow speeds through prominent terrain gaps such as the Cajon Pass (leading to

[1] Examples: On 21 October 2007, the weather station on Laguna Peak, overlooking Pt. Mugu, recorded a 50 m s^{-1} (111.5 mph) wind gust. More recently, on 30 April 2014, a station in San Diego County (Sill Hill, SILSD) reported a 45 m s^{-1} (101 mph) gust, and remained above 40 m s^{-1} (90 mph) for a total of five nonconsecutive hours.

Corresponding author address: Robert Fovell, Atmospheric and Oceanic Sciences, University of California, Los Angeles, 405 Hilgard Ave., Los Angeles, CA 90095.
E-mail: rfovell@ucla.edu

DOI: 10.1175/MWR-D-15-0147.1

Santa Ana) and through the Soledad Pass (northwest of Los Angeles), creating prominent wind corridors in the northern part of the Los Angeles basin (Jackson et al. 2013). Wind speeds can also be very large in San Diego County, where the terrain gaps appear less prominent but mountain heights are also generally lower. The flow across this topography shares many characteristics of classic downslope windstorms (e.g., Huang et al. 2009).

Downslope windstorms are a type of large-amplitude mountain wave that can produce strong, often gusty winds on the lee side of a mountain barrier (Durran 1990, 2003; Jackson et al. 2013). They are observed in many areas of the world, and carry such names as the bora, chinook, foehn, zonda and taku winds (e.g., Schamp 1964; Durran 2003). Windstorms require a sufficiently large mountain barrier, and a terrain-dependent magnitude of cross-barrier winds, along with another ingredient such as an elevated inversion (e.g., Vosper 2004; Sheridan and Vosper 2006), Scorer parameter layering (e.g., Durran 1986), or a critical level either associated with the mean state (e.g., Durran and Klemp 1987) or generated by wave breaking (e.g., Peltier and Clark 1979). Subsidence associated with downslope windstorms can cause very low relative humidities near the surface, particularly if the air mass starts with low absolute humidity.

In complex terrain, the wind can vary greatly over small distances and gustiness is common in downslope windstorms, which may include rotors and subrotors embedded in the flow (Doyle and Durran 2004; Jackson et al. 2013). Terrain-amplified winds and gusts can knock down trees and power lines, starting and spreading fires, making accurate forecasts in this region extremely important. Proper model verification, however, can be hampered by the sparseness of the surface network, the absence of stations in wind-prone areas, as well as deficiencies in anemometer placement. As an example, on 21 October 2007, the Witch Creek fire was sparked by wind-whipped power lines located about 20 m above ground level (AGL), and was driven by an especially strong Santa Ana winds to become one of the largest fires in California history.[2] It is nearly certain that the meteorological stations that existed at the time did not fully capture the ferocity of the winds experienced at the initiation site of that or other fires that started during this windstorm.

[2] According to information obtained from the California Department of Forestry and Fire Protection (Cal Fire), the Witch Creek fire was the third largest California wildfire since 1932 upon its containment, and is ranked sixth largest as of this writing.

Despite steady improvement in operational numerical weather prediction models over the last several decades as well as advancements in the understanding of mountain meteorology dynamics, forecast skill for downslope windstorms is still limited by several factors, including dependence and/or sensitivity to model resolution (e.g., Reinecke and Durran 2009b; Jackson et al. 2013), numerical schemes (e.g., Reinecke and Durran 2009b), vertical coordinates and diffusion (e.g., Smith et al. 2007), physical formulations [especially the boundary layer; see Smith (2007)] and initial condition uncertainties (e.g., Reinecke and Durran 2009a). Our work was motivated by the need to forecast winds that could affect electrical transmission lines in San Diego County operated by the San Diego Gas and Electric (SDG&E) company. Operational products were viewed by the meteorologists tasked with anticipating wind threats in the electric network as insufficiently skillful (B. D'Agostino and S. Vanderburg 2012, personal communication). In particular, even available high-resolution (4-km horizontal grid spacing or better) products permitted the strong near-surface winds to extend downslope too far and too often, resulting in false alarms and a waste of resources.

In this part, we examine the skill of the Advanced Research version of the Weather Research and Forecasting (WRF) Model (Skamarock et al. 2008) core in forecasting Santa Ana winds in San Diego County. High spatial resolution is focused over this area, especially over the area's roughly north–south mountain range that serves to amplify the winds. Model forecasts are verified against wind observations reported by the SDG&E mesonet, a recently installed and exceptionally dense surface observing network of (presently) more than 140 stations sited primarily in well-exposed, wind-prone areas on the west-facing slopes of the county's mountains. Numerous combinations of model physical parameterizations were examined, for this and similar events, to identify the configuration that best captures the magnitude, temporal evolution, and spatial extent of the winds. Although the verification observations are still confined near the surface, we will show that the SDG&E network helps reveal model weaknesses and suggest remedies that might not have been detectable from a less-extensive set of observations.

The structure of this paper is as follows. The available observations, model experimental design, and verification strategy are presented in section 2. The mid-February 2013 event is described via SDG&E network observations in section 3. Section 4 presents the model simulations and comparisons with the observations, and the summary composes the final section.

2. Data and methods

a. Available observations

Observations are crucial for vetting a numerical model, but there are several significant challenges involved. First of all, most of the data available for verification are located very close to the surface, and even these have historically been relatively sparse. With respect to airflow, the relevant information comes in the form of "sustained winds," which are temporally averaged quantities composed of discrete samples measured by anemometers. While the WMO (2010) provides some guidelines for sustained wind collection at synoptic stations (specifying a 10-m anemometer mounting height above local open ground and removed from obstacles, and a 10-min averaging period), it remains that networks tend to differ with respect to sensor hardware, mounting height, station siting guidelines and sampling, and averaging and reporting intervals. All of these can dramatically impact the magnitudes of winds and gusts that are reported, complicating the verification process.

As an example, most (not all) ASOS stations report sustained winds at 10 m AGL, but averaged over a 2-min period, with data available at 1-min intervals (NOAA 1998).[3] The WRF provides a wind diagnostic for this height, which typically resides between the lowest model level and the surface. However, most available measurements in complex terrain come from the Remote Automated Weather Stations (RAWS) network that employs anemometers mounted closer to the surface (6.1 m AGL) and transmit longer (10 min) averages for the sustained wind once per hour (leaving over 80% of the hour unsampled). Thus, regardless of other factors, contemporaneous and collocated RAWS and ASOS sustained wind reports can be expected to disagree. In verification exercises, adjustments dependent on vertical stability and surface roughness have to be made to the model's standard 10-m wind diagnostic to avoid a potentially false conclusion of overprediction.

The WMO (2010) notes that "the most difficult aspect of wind measurement is the exposure of the anemometer." Even a cursory examination of RAWS site photos hosted by the Desert Research Institute (DRI)[4] reveals numerous examples of problematic anemometer placement with respect to buildings and/or trees. During the aforementioned Witch Creek fire, the RAWS station at Goose Valley (GOSC1) occupied an important location immediately downwind and downslope from the ignition location, but at the time was closely surrounded by significant obstacles (verified by inspection). It is not known how much larger its event maximum sustained wind (15 m s^{-1}) and gust (25 m s^{-1}) might have been had the station not been sited close to large trees.

Since 2009, SDG&E has deployed surface stations in wind-prone areas across San Diego County (Fig. 1). Sites were carefully selected in order to accurately and properly gauge the wind threat to well-exposed electrical installations. These stations conform to the RAWS standard (National Wildfire Coordinating Group 2014) with respect to anemometer height (20 ft or about 6.1 m AGL) and sustained wind formulation (10-min averages from 3-s samples), but report every 10 min instead of hourly. For each 10-min interval, the sample resulting in the largest wind speed is reported as the gust. Station identifiers consist of five characters, terminating with "SD." (This suffix will be ignored when convenient.)

As a test, SDG&E station GOSSD was purposely placed at a better-exposed location 0.7 km along Black Canyon Road from GOSC1's original location.[5] For the month of December 2011, which included several moderate Santa Ana wind events, the 10-min-averaged sustained winds at GOSSD were about 50% stronger than at the more sheltered RAWS station (Fig. 2), even though they were measured at the same height. Indeed, among the 744 contemporaneous observations of sustained wind during that month, 639 SDG&E observations were larger than their corresponding RAWS wind speed, 48 observations were the same, and only 56 of the RAWS observations (<8% of the total) exceeded the SDG&E reports. As demonstrated clearly below, even closely spaced and well-exposed stations can exhibit wind variability of this magnitude, so part of the GOSSD-GOSC1 discrepancy might have been due to an unappreciated terrain effect. However, this result motivated us to use the SDG&E network exclusively to verify our model results, owing to its high density and optimal siting philosophy. The purpose of our work, after all, is to forecast winds impinging upon electrical lines at risk of igniting wildfires in well-exposed terrain.

b. Model experimental design

The simulations examined herein were made using WRF version 3.5. To represent an operational environment, the model was initialized with the North American Mesoscale Forecast System (NAM) gridded

[3] The sampling interval for these stations was shortened from 5 to 3 s between 2005 and 2009 (Tyner et al. 2015).

[4] http://www.raws.dri.edu.

[5] Prior to November 2011, GOSSD was sited even closer to GOSC1, in a less well-exposed area intended to mimic the RAWS siting issues (S. Vanderburg 2012, personal communication). GOSC1 was subsequently moved.

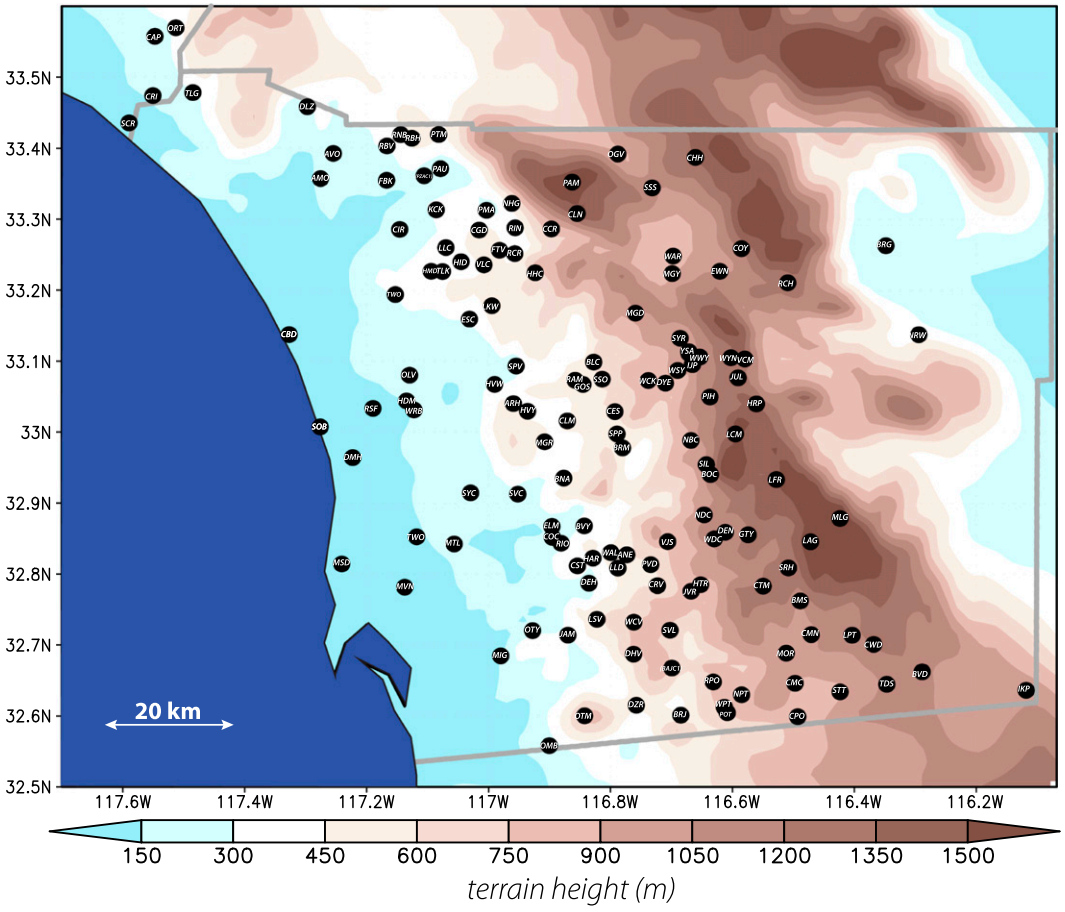

FIG. 1. SDG&E surface station locations (black dots), with underlying topography shaded. Station labels omit "SD" suffix. Stations were in place as of February 2013.

analysis and forecasts from its 1200 UTC 14 February 2013 cycle, and integrated for 54 h. A five-domain telescoping grid arrangement (denoted D1–D5) is used with horizontal grid spacings of 54, 18, 6, 2, and 0.667 km, respectively (Fig. 3). The innermost 667-m nest extends about 80 km west–east by 70 km north–south and covers roughly 70% of the SDG&E mesonet, while its parent 2-km grid encompasses the entire network. The highest resolution (~10 m) U.S. Geological Survey (USGS) terrain database available was used in the construction of the topography of the innermost two domains,[6] permitting the model to capture finer-scale features (see Fig. 3 inset) than the USGS database distributed with WRF makes possible.

The model top is 10 hPa, with 50 layers (51 full-sigma vertical levels) employed, focusing the highest resolution in the lower troposphere in the usual fashion. By default, the WRF real-data initialization program (real.exe) places about 7 half-sigma (wind and scalar) levels in the lowest kilometer AGL, with the first level (Z_a) at about 27 m above the surface. The placement of the lowest model wind level can influence surface fluxes (Wei et al. 2001), modulate the operation of the planetary boundary layer (PBL) scheme (Shin et al. 2012), and have a particularly strong impact on downslope windstorms (Zängl et al. 2008). We utilize the default setup of Z_a = 27 m for the simulations referenced herein, for the reasons discussed in section 2c.

Although it provides no information above 6.1 m AGL, the exceptionally dense SDG&E surface observation network enables us to evaluate the realism of the model simulations of the terrain-amplified winds. This is important, as we have determined from many hundreds of WRF simulations of this and other events that important local and county-wide characteristics of the downslope flow are quite sensitive to resolution, land-use assumptions, model physics, and even random noise (cf. Cao 2015). Our experiments for each event have included combinations of 5 land surface models (LSMs)

[6] http://nationalmap.gov/viewer.html.

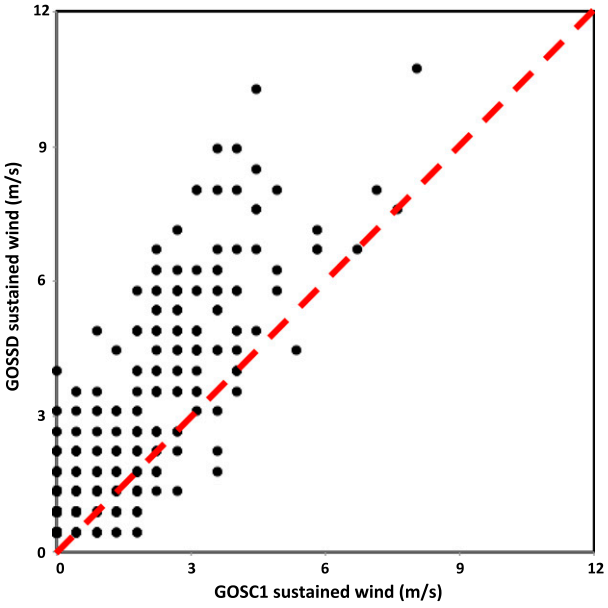

FIG. 2. Scatterplot of hourly sustained winds measured at the Goose Valley RAWS (GOSC1) and SDG&E (GOSSD) sites for December 2011, with a 1:1 correspondence line (red). Owing to rounding, there are numerous overlapping observations.

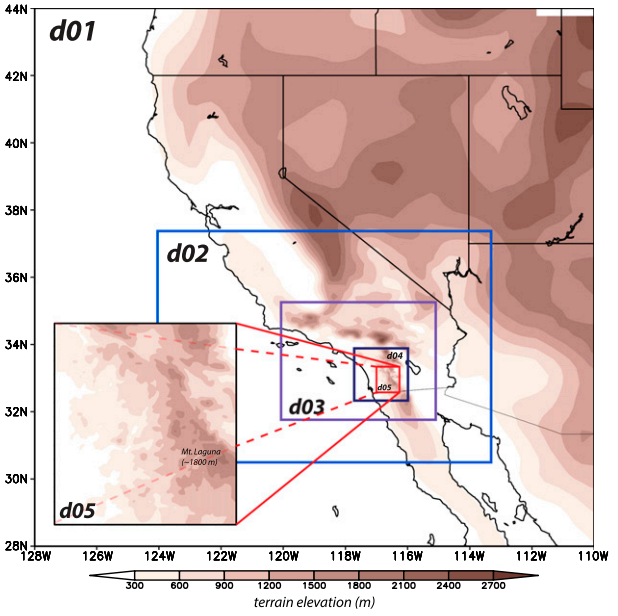

FIG. 3. Domain configuration for the WRF simulations, with topography shaded. Domains 1–5 employ horizontal grid spacings of 54, 18, 6, 2, and 0.667 km over Southern California, respectively. The inset shows an enlarged version of domain 5.

and 10 PBL schemes as well as 2 land-use databases (USGS and MODIS); for each PBL scheme, the recommended and/or most frequently adopted surface layer parameterization was employed. Simulations were nearly insensitive to some other physics options, such as the microphysics and cumulus schemes (Cao 2015).

The physics combination that consistently best represented the sustained wind observations over a set of events with respect to magnitude and temporal and spatial variation employed the Pleim–Xiu (PX; Pleim and Xiu 1995; Xiu and Pleim 2001) LSM and surface layer scheme, along with the Asymmetric Convection Model, version 2 (ACM2; Pleim 2007a,b) PBL parameterization. This "standard" configuration, labeled PX–ACM2, also utilized the MODIS land-use database, the Rapid Radiative Transfer Model for General Circulation Models (RRTMG; Iacono et al. 2008) radiation parameterization, and explicit horizontal diffusion was not applied. Neither the land-use nor diffusion choice had much impact on the results (Cao 2015) for this combination.

While the physics sensitivity experiment will be explored more fully in Part II, we will also reference herein results using the Noah (Chen and Dudhia 2001; Ek et al. 2003) and thermal diffusion (TD; Skamarock et al. 2008) LSMs, and the Yonsei University (YSU; Hong et al. 2006), Mellor–Yamada–Janjić (MYJ) PBL scheme (Janjić 1994), and total energy–mass flux (TEMF; Angevine et al. 2010) PBL parameterizations. In particular, the Noah–YSU combination, along with the surface layer scheme derived from MM5 (Noah–YSU),[7] is of interest because it is likely the most commonly used configuration in WRF.

c. *Verification strategy*

As noted above, SDG&E stations were intentionally placed at wind-prone sites. An unavoidable assumption being made in this study is that the SDG&E stations are representative of the landscape as a whole—or at least as it is rendered in the model. At a given grid spacing, the model is trying to capture the gross features of the terrain, which enter into parameterizations such as the LSM via such factors as the surface roughness length. It cannot directly incorporate subgrid-scale features such as trees, buildings, small hills, and terrain creases that can act to locally modulate the wind in the immediate vicinity of an anemometer. We believe that one advantage of SDG&E observations over their RAWS counterparts is that they are less likely to be influenced by small-scale features that we know we cannot represent on the grid, and thus may be more representative of the landscape we are capable of resolving.

SDG&E mesonet observations were obtained from the Meteorological Assimilation Data Ingest System (MADIS) archive and interpolated to station locations using the Developmental Testbed Center's MET

[7] This surface scheme was modified for WRF, version 3.6.

software. For wind, we compared instantaneous model predictions computed on the hour with sustained wind observations, which is the standard (if not often explicitly acknowledged) practice. Comparisons of model winds with observed gusts are not appropriate because the model's resolution, configuration, and filters preclude its ability to resolve small-scale turbulent motions. In theory, model fields could be averaged over time periods comparable to the sustained wind averaging period, but in practice this makes very little difference. The goal is to faithfully capture the overall temporal evolution and spatial characteristics of the event.

WRF computes a wind diagnostic relating the lowest model level wind V_a at height $z = Z_a$ to the WMO standard height of 10 m ($V_{10\mathrm{m}}$) via the logarithmic wind profile assumption (e.g., Oke 1987):

$$V_{10\mathrm{m}} = V_a \frac{\ln\frac{10}{z_0} - \psi_{10\mathrm{m}}}{\ln\frac{Z_a}{z_0} - \psi_a}, \tag{1}$$

where z_0 is the surface roughness length, and ψ_a and $\psi_{10\mathrm{m}}$ represent stability correction functions at Z_a and 10 m that vanish when the surface layer is neutrally stratified. However, proper comparison with the SDG&E network winds requires further adjustment to its anemometer mounting height at 6.1 m AGL level ($V_{6.1\mathrm{m}}$), that is,

$$V_{6.1\mathrm{m}} = V_{10\mathrm{m}} \frac{\ln\frac{6.1}{z_0} - \psi_{6.1\mathrm{m}}}{\ln\frac{10}{z_0} - \psi_{10\mathrm{m}}}, \tag{2}$$

where $\psi_{6.1\mathrm{m}}$ is the stability correction computed at anemometer level.[8] Although somewhat dependent on the land surface model and surface layer scheme, land-use database (e.g., USGS vs MODIS) employed and season, z_0 values range between 0.05 m and 0.9 m at SDG&E stations, resulting in wind speed reductions of 10%–20% from the 10-m values even when conditions are neutral.

An acknowledged limitation of this study is our assessments are being made solely with near-surface observations and presume a wind profile [Eq. (2)] that is implicitly or explicitly relied upon (e.g., Mass et al. 2002), but not well tested (cf. Stensrud 2007), in complex terrain. An alternative to the latter would be to shift the vertical coordinate so the lowest model wind level resides at $Z_a = 6.1$ m, permitting a direct comparison with the observations. This has been investigated for a number of events, but we have found that 1) shifting PX–ACM2 did not change its forecast skill very much; 2) PX–ACM2 retained its skill advantage relative to other physics combinations, even after shifting; and 3) most importantly, the shifted PX–ACM2 setup encountered linear instability issues in a subset of events (including the one examined herein) necessitating the use of much smaller time steps. As a consequence, we retain the default Z_a placement for this study. Finally, it is noted that Eqs. (1) and (2) could have been written with the zero-plane displacement modification of the anemometer heights that is sometimes used in areas with significant obstacles; we neglect this adjustment because most SDG&E stations were installed in well-exposed areas.

Event-averaged mean absolute error (MAE) and bias statistics, defined for station j and time i as

$$\mathrm{MAE} = |f_{j,i} - y_{j,i}| \tag{3}$$

and

$$\mathrm{bias} = (f_{j,i} - y_{j,i}) \tag{4}$$

are employed as tools to measure how close pointwise model predictions f_i are to their corresponding observations y_i. Model gridded winds are first interpolated to the SDG&E station locations using hourly information,[9] representing the initial time and 54 subsequent forecasts. From these data, network averages for each verification time are computed, and the event-averaged MAE and bias represent the mean network average over the 55-h event window. Using these measures, we will show that most model physics configurations generate a high wind bias relative to the observed sustained winds, even after anemometer or model level height adjustment, with the worst offenders ostensibly being those employing the MYJ PBL. However, we discovered the MYJ code was recomputing the 10-m wind values, specifying smaller roughness lengths than actually employed in the model integrations. This purely cosmetic adjustment, shared by the QNSE PBL scheme (Sukoriansky et al. 2006), exacerbated the high

[8] Neutrality is often presumed when wind speeds exceed about 5 m s^{-1} or so (e.g., Wieringa 1976; Verkaik 2000), which does appear valid among our model simulations. The stability corrections in Eq. (2) were retained for simulations examined in detail in this report, but these was found to have relatively little impact on the results and no influence on the conclusions.

[9] Mesonet data were obtained at full temporal (10 min) resolution and we elected to replace observed winds on the hour with the largest values reported during the previous 50 min, motivated by the relatively larger high-frequency variability present in the observations and our practical concern with the high wind threat. However, this was found to have relatively little impact on the results and no influence on the conclusions.

wind bias, and removing the code (as done for this study) made physics ensemble members employing MYJ and QNSE much more competitive.

3. The 14–16 February 2013 event observations

Although only moderate in overall strength as a Santa Ana episode, some very impressive winds ($\sim$26 m s^{-1}) and gusts ($\sim$41 m s^{-1}) were recorded in the SDG&E network during the 14–16 February 2013 event. More interestingly, this event was a two-phase episode, with the first phase characteristic of the development of a well-developed hydraulic jumplike feature associated with wind reversals, and the second one being a normal downslope progression of winds.

Certain synoptic-scale conditions interacting with local topography contribute to Santa Ana occurrence (Yoshino 1975; Sommers 1978; Hughes and Hall 2010). This mid-February Santa Ana wind event commenced around 0000 UTC 15 February 2013, as maximum sea level pressures exceeded 1028 hPa in the Great Basin (Fig. 4a), and a midlevel ridge approached the western United States, bringing northeast winds over the mountains encircling Southern California (Fig. 4d). Some stations reported their fastest offshore winds around 1800 UTC 15 February 2013, when the Great Basin high and the 700-hPa ridge reached peak magnitudes (Figs. 4b and 4e). During the next 24 h, the high pressure migrated eastward (Fig. 4c), away from Southern California, the surface offshore winds weakened, and the 700-hPa ridge flattened (Fig. 4f).

Figure 5 presents the maximum wind gusts observed in the SDG&E network for the event. The strongest gusts are found to be located along the western slopes, close to but not at the ridgelines. The great spatial variability of the winds can be detected in Fig. 5b, which focuses on the ''central area'' that comprises the stations of greatest present interest. Peak gusts varied between 10 and 30 m s^{-1} within a 5-km distance, suggesting each station is representative only of a small local area, at least with respect to the winds. The event-maximum sustained winds (not shown) are similar in pattern although naturally weaker in magnitude.

Figure 6a presents a time series of winds and gusts recorded at central area stations Sill Hill (SIL) and Boulder Creek (BOC). The event as a whole was characterized by two peaks separated by a protracted lull that occurred during the afternoon and early evening hours of 15 February. At 1830 UTC (1030 PST) on 15 February, SIL recorded a 41 m s^{-1} wind gust, at a time when no other stations in this region had a gust exceeding 26 m s^{-1}. Indeed, the winds were 50% weaker at BOC, which is just 1.6 km to the south (Fig. 5b). (Keeping in mind that the sustained wind represents 10-min averages and the gusts are single 3-s samples, note how similar the sustained wind at SIL is to the wind *gusts* from BOC.) It would be easy to dismiss such a high wind observation, but the station record shows that gusts exceeding 36 m s^{-1} were frequently recorded occurrence (Fig. 6a), and eye-level gusts of 33 m s^{-1} had been measured with hand-held anemometers at the site about an hour earlier (B. D'Agostino and S. Vanderburg 2013, personal communication). A close inspection of the topography in the vicinity of SIL and BOC (not shown) indicates that SIL is sited on a small local ridge while BOC resides in a narrow terrain crease, very small-scale features that may be relevant to the wind speeds and exposures and illustrate the challenge that is faced in simulating and verifying the winds across this area.

We now shift focus to the Witch Creek (WCK) area, where the SDG&E station density is particularly high (Fig. 5b). At West Santa Ysabel (WSY; Fig. 6b), located on the west-facing slope about 9–10 km down from the ridge, gusts during the first phase peaked at 26 m s^{-1} at 1800 UTC (1000 PST) on 15 February and regained comparable strength by midnight local time before finally slowing as the event wound down. Although about 40% weaker than the gusts, the sustained winds at WSY followed a similar trend. At SDG&E station Julian (JUL), close to the ridge, the gusts were much weaker than WSY's during the first phase, stronger (although still fairly slow) during the afternoon lull, and markedly weaker again during the second phase. This hints that there is something structurally and/or dynamically different about the second half of the event.

The winds also behaved very differently at the WCK station (Fig. 6c), which is less than 5 km downslope from WSY. Through the first phase, WCK's gusts remained much weaker than WSY's. Note the wind direction at WCK occasionally reversed to upslope (at times indicated by the black dots) during this period, including at and around the time of WSY's peak gusts. During the lull between the two phases, the WSY and WCK winds were comparably weak. While the winds remained downslope at WCK during the lull, they often reversed to upslope at WSY (at times indicated by the gray squares). Wind reversals reappeared at WCK during the onset of the second phase before downsloping became firmly reestablished there. WCK recorded its event maximum gust of 23 m s^{-1} at 1130 UTC 16 February, during the second pulse and about 3 h after the winds at WSY started to decline.

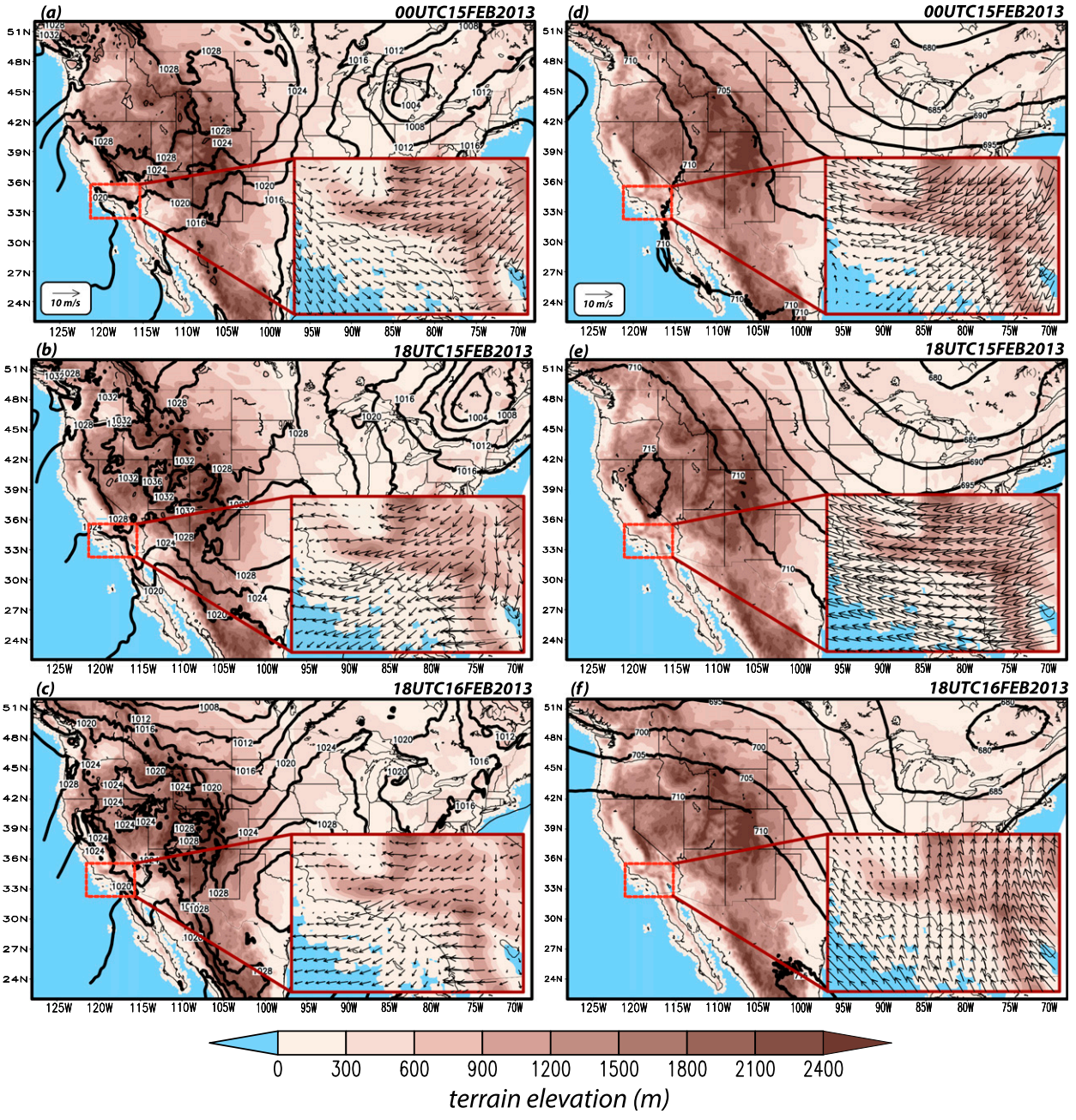

FIG. 4. NAM model sea level pressure analyses for (a) 0000 UTC 15 Feb, (b) 1800 UTC 15 Feb, and (c) 1800 UTC 16 Feb 2013; and 700-hPa analyses for (d) 0000 UTC 15 Feb, (e) 1800 UTC 15 Feb, and (f) 1800 UTC 16 Feb 2013. The insets show the total (left) 10-m and (right) 700-hPa winds of Southern California (the red box). Only a subset of vectors are plotted for clarity. Topography is shaded.

Station Sunset Oaks (SSO) is located 7 km farther downslope from WCK. Note that, during the first pulse, its gusts were weaker than, but in phase with, WSY's. The wind reversals at WCK during this time occurred with while downslope flow was observed both uphill (at WSY) and downhill (at SSO), indicating a rotor or jump may have formed there. The upslope shift of the wind reversals during the lull period from WCK to WSY could be explained by a change in the rotor or jump position. Station SSO emerged last from the lull, and its second peak was reached after the gusts at both WSY and WCK had started to decline. Taken together, these stations suggest a two-part Santa Ana event in which winds were largely in phase early in the event, apart from the suspected jump at WCK, and had a second pulse

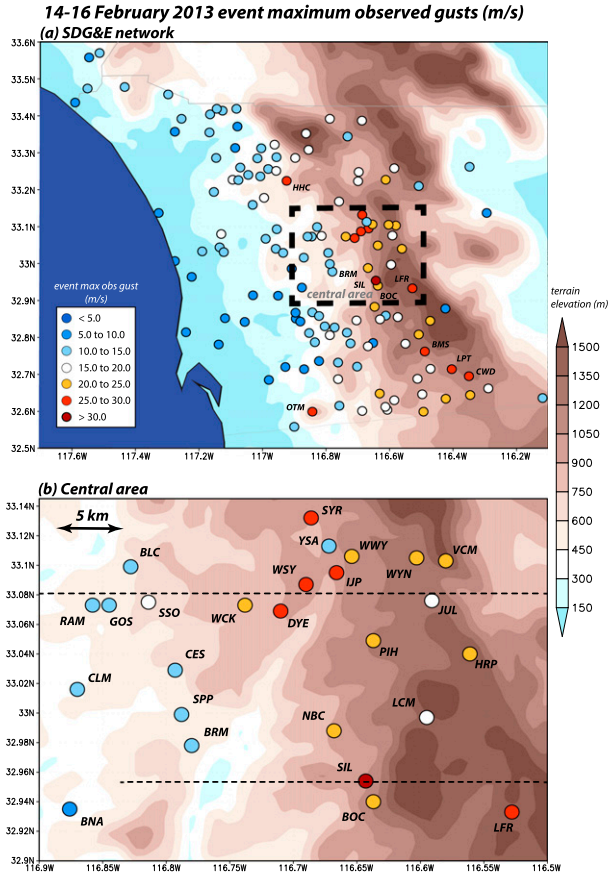

FIG. 5. Spatial distribution of 14 Feb 2013 event maximum observed wind gusts ($m\,s^{-1}$) with topography (shaded) for SDG&E stations in (a) the entire network and (b) the central area identified in (a). Black dotted lines denote locations of cross sections across WSY and SIL shown in Figs. 13 and 15.

consisting of a marked downslope progression as the overall winds abated.

4. Model simulations and verifications

In sections 4a–c, the standard run is verified and examined, and its configuration is justified.

a. *Verification of the standard run*

To a large extent, the standard PX–ACM2 simulation captured the magnitude and temporal evolution of the SDG&E network-averaged sustained winds (the mean of 138 sites), at least after the first 12 h (Fig. 7). Over the entire simulation period, the linear correlation between the network-averaged hourly observations and forecasts was 0.85, and the network- and event-averaged MAE and bias were 2.23 and 0.07 $m\,s^{-1}$, respectively. Individual stations having relatively large and small errors or biases are ostensibly dispersed randomly in space (Fig. 8). Like the network as a whole, the spatially averaged bias is nearly zero in the aforementioned central area, although clearly very variable in space (Fig. 9), so that overpredicted stations reside in close proximity to underpredicted ones. This hints at the value of high network density and the danger of drawing conclusions from a limited number of stations.

However, these plots may obscure some potentially important aspects of the sustained wind reconstructions. Among the 138 stations employed in the verification, MAE is positively correlated with the event-averaged observed wind (Fig. 10a; $R^2 \sim 0.5$ for the red curve) while the bias is negatively related (Fig. 10b; $R^2 \sim 0.5$ for the red line) to the wind. Both of these relationships are largely driven by the stations recording the highest wind speeds, and are much smaller ($R^2 \sim 0.1$ and 0.2, respectively), although still significant at the 99% level, if the windiest 10 locations (7% of the network) are removed. The uniqueness of the windy station subset can be seen when MAE and bias are presented in rank order (Figs. 10c,d); the majority of the locations (indicated by the red dots) comprise the blades of hockey stick–like structures. Six of these high-wind stations (SIL, LFR, VCM, BOC, HRP, and IJP) reside in the central area (Fig. 9).

Still, if the windiest locations are excluded, the network- and event-averaged MAE and bias are only slightly changed (to about 2.1 and 0.4 $m\,s^{-1}$, respectively). Furthermore, we will show later (in section 4c) that this result is a common characteristic of Santa Ana WRF simulations overall, independent of model physics and not unique to this event, so that exclusion of the windy subset would not alter our findings. Instead, it does not appear possible to accurately predict the winds at the windiest locations without simultaneously overpredicting the wind speed nearly everywhere else. The standard model configuration was selected to maximize network-averaged skill at reproducing the 6.1-m wind integrated over the network and through the event (as well as through other episodes not explicitly considered herein). It needs to be borne in mind that the model will require bias correction at the most wind-favored locations.

b. *Spatial and temporal variation of the winds in the standard run*

Figure 11 (left column) compares hourly time series of simulated sustained wind at stations WSY, WCK, and SSO, with the observations used in the verification. Overall, the simulation captures the evolution and magnitude of the winds at each station to a good degree, although there are some clear timing issues. At WSY, the magnitude of the second pulse was underpredicted, although the phasing was skillful (Fig. 11a). The second phase's winds ramped up too early at both

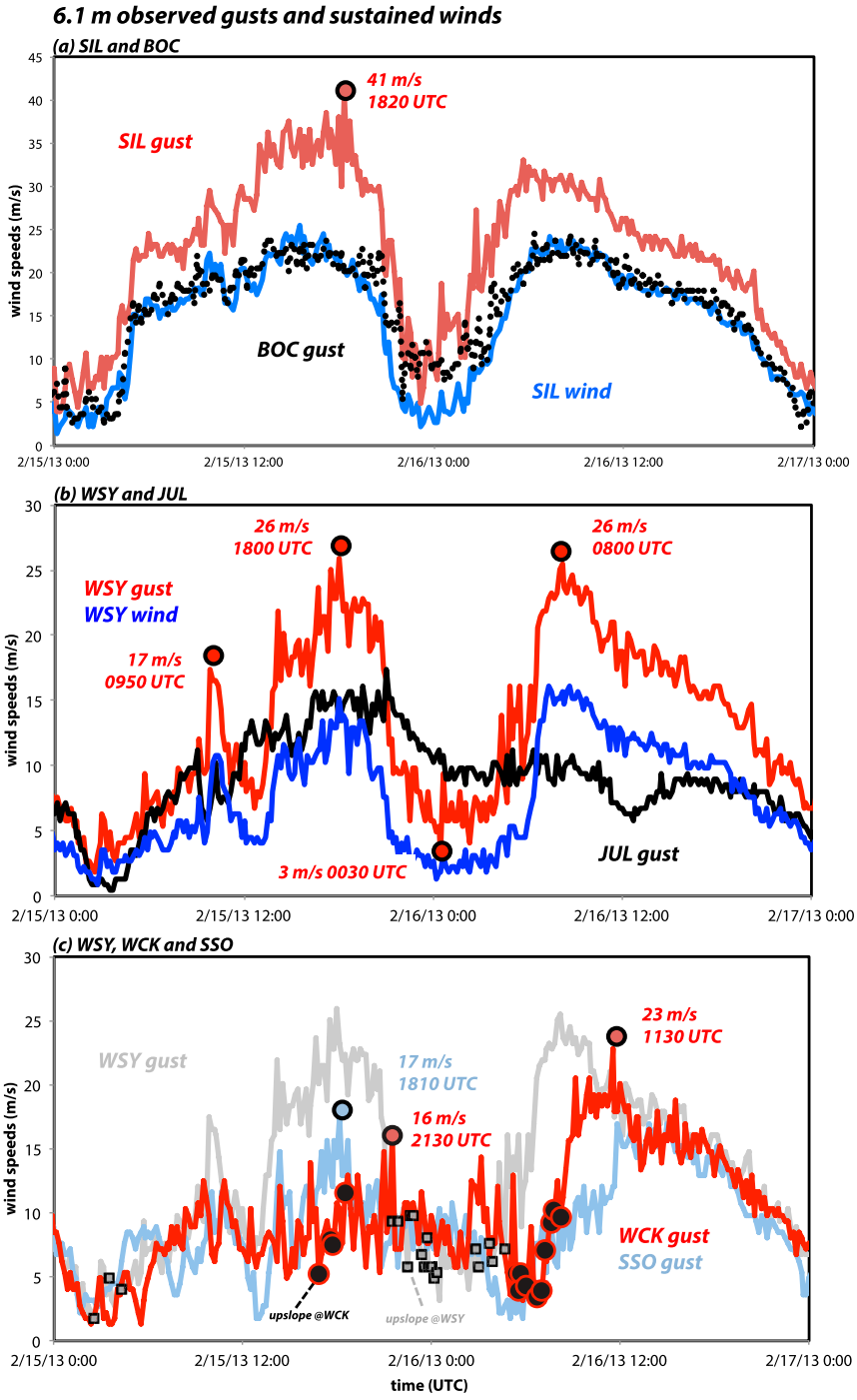

FIG. 6. Time series of observed gusts and sustained winds ($m\,s^{-1}$) over 2 days at (a) SIL and BOC; (b) WSY and JUL; and (c) WSY, WCK, and SSO. Some maxima and minima are highlighted. In (c), black dots indicate times when winds were directed upslope at WCK and gray squares indicate times when winds were directed upslope at WSY.

WCK and SSO (Figs. 11b and 11c). That said, however, the model captured the overall event evolution (Fig. 11d) as manifested by the observed winds (Figs. 11a–c) and gusts (Fig. 6c): during the first pulse, wind speeds remained markedly weaker at WCK than at stations both upslope and downslope, and the second pulse was characterized by a downslope progression of the flow with time.

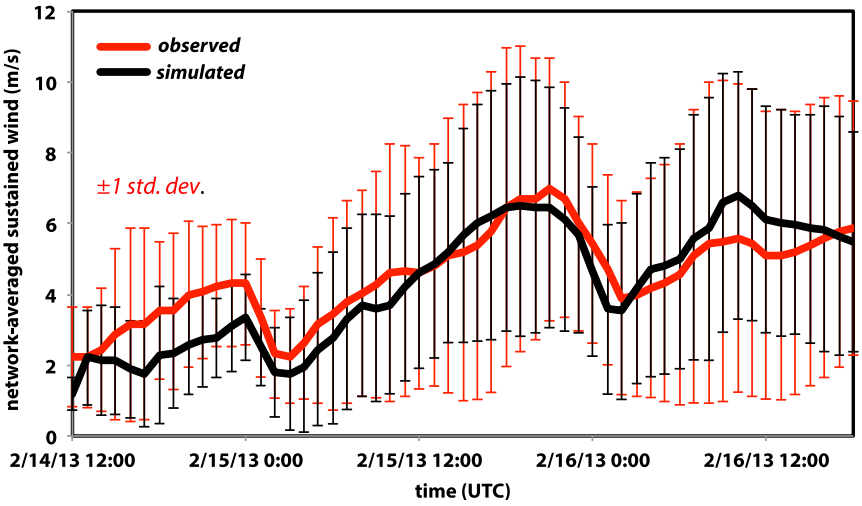

FIG. 7. Time series of SDG&E network-averaged sustained wind ($m\,s^{-1}$) observations (red line) at 6.1 m AGL over 2 days, for comparison with predictions from the standard (PX–ACM2) run (black line). Red and black color bars are plus and minus one standard deviation for observations and the standard run, respectively. The plot spans the entire 54-h simulation period.

Having demonstrated reasonable fidelity with the available observations, the simulation will be used to complete the horizontal wind field (Fig. 12), and provide insight into the vertical dimension that is missing from the observations (Figs. 13 and 15). By 0800 UTC 15 February 2013 (Fig. 12a), the downslope windstorm had already started, but the winds near the ground at WSY and stations farther downslope had not yet begun to rise. The model indicates that significant easterly flow was already present above WSY and WCK, but had not yet reached the surface (Fig. 13a). Recall that by 1740 UTC, winds recorded at WSY and SSO had reached their first-phase peaks, but WCK's winds remained quite weak (Figs. 6c and 11b). The simulation has indeed developed a jumplike feature almost directly above WCK at this time (Fig. 13b), rendering relatively weak winds there and upslope nearby (see the square and blue arrows in Fig. 12b). The reversed upslope winds indicate the existence of a local horizontal roller and characterize a turbulent and clearly defined hydraulic jump (e.g., Chanson 2009). Note also that, as expected, the wind speeds had not strengthened very much at JUL, which is located at the top of the ridge and at the very edge of the terrain-induced flow amplification.

Five hours later, there was a brief period (around 2130 UTC) during which the observed gusts at WCK were actually stronger than at the other stations (Fig. 6c), having reached their first-phase peak of $16\,m\,s^{-1}$. The winds at WSY and SSO had already entered the lull period, and the wind at WSY was directed upslope at and after this time. While the timing is not perfect, the model suggests this occurred as the jumplike feature retreated upslope, relocating the reversed flow to WSY (Fig. 13c; see square in Fig. 12c). As the windstorm subsequently retreated even farther eastward, it also weakened and became more elevated (Fig. 13d). The model reveals that strong near-surface winds still existed during the lull, but became concentrated close to the ridge and in an area where there were no stations (see between WSY and JUL in Figs. 12d and 13d).

The second phase of the Santa Ana event ensued as the reintensifying flow began progressing downslope again after 0500 UTC 16 February (Figs. 13e and 12e). Note another, smaller-amplitude jump formed in the vicinity of WCK, again consistent with the wind reversals seen in the observations (Fig. 6c). By midnight local time (0800 UTC), however, that feature had disappeared and the downsloping flow became "flatter" and, eventually, shallower as the Santa Ana event eventually wound down (Figs. 13f–h). The observations indicated that a westward and downslope progression in the peak near-surface wind speeds (Fig. 6c) had occurred, and the model has largely captured this behavior (Figs. 11d and 12f–h).

The retreat separating the two phases likely responds, at least in part, to temporal variations upstream of the mountain ridge, some of which are diurnal in character and some are associated with the evolution of the synoptic-scale environment. Figure 14 presents a time versus height view of stability and temperature (at top) and winds (at bottom) at the location marked "E" in Fig. 13, just east of the ridge. The figure reveals that an elevated inversion atop a less

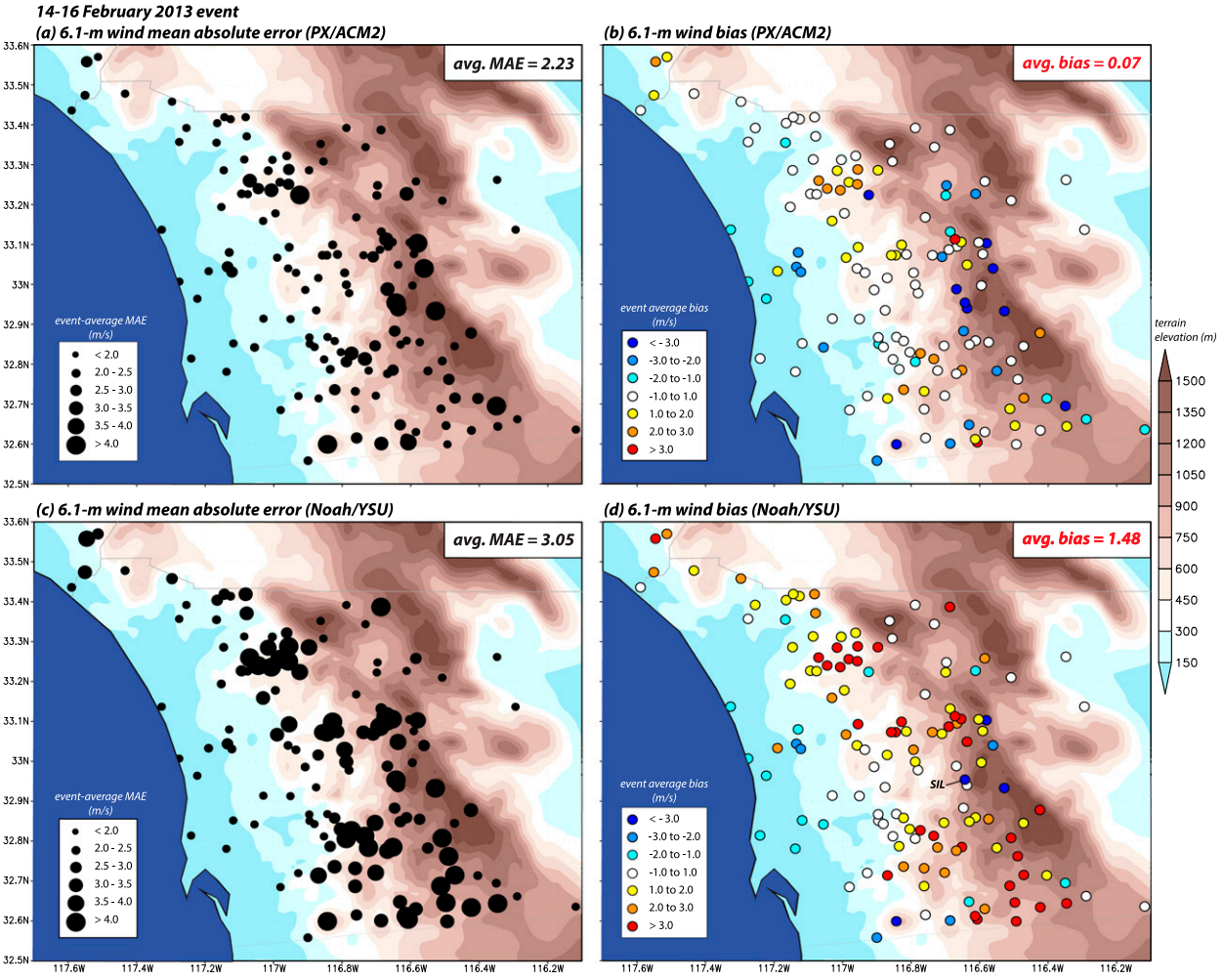

FIG. 8. As in Fig. 5a, but for (a) event-mean sustained wind MAE against observations and (b) event-mean sustained wind bias against observations, for the standard simulation. (c),(d) As in (a),(b), but for the Noah–YSU run.

stable layer was present through most of the Santa Ana episode, similar to the situation studied by Vosper (2004). Elevated inversions also occur during high-wind events at Boulder, Colorado (e.g., Brinkmann 1974; Klemp and Lilly 1975). The inversion had appeared prior to 0000 UTC 15 February, and the winds just east of the ridge had already acquired an easterly component, but the simulated winds at WSY (superposed for reference) did not rise until the inversion and cross-ridge flow both strengthened during the next 12 hours.[10]

After the maximum winds were reached at WSY, note that the easterlies above point E subsequently changed relatively little through 0600 UTC 16 February, spanning the entire interperiod lull. While a closer examination is required, the windstorm's upstream retreat appears to be associated with the erosion and descent of the inversion that occurred after 1800 UTC on the 15th, in the hours after sunrise (around 1430 UTC). Part of this evolution is a consequence of daytime heating, which is evident in the evolution of the temperature contours below about 3.5 km MSL (2.4 km AGL) in Fig. 14a. The increasing separation between the 298- and 306-K isentropes in Fig. 14b during this time is also consistent with surface-based heating, and indicative of a weakening and repositioning of the inversion.

The second phase commenced after the inversion again ascended after 0400 UTC 16 February, a few hours after sunset (around 0130 UTC). Through the second

[10] A critical level with respect to the cross-ridge wind appeared above 4 km above mean sea level (MSL) prior to WSY's first peak, but did not persist. A mean state critical level was present at 7 km MSL throughout the event; not shown.

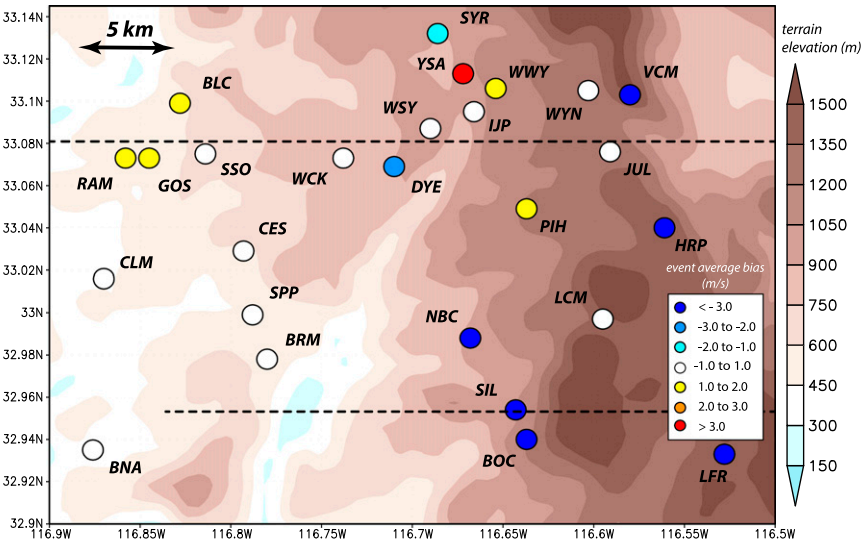

FIG. 9. As in Fig. 8b, but zoomed into the central area. Labels indicate names of SDG&E stations, with the "SD" suffix omitted. Black dotted lines denote cross sections across WSY and SIL shown in Figs. 13 and 15.

pulse, however, the easterly winds were not only weaker but also located closer to the surface, and the stability structure evolved further, becoming surface based after sunrise on 16 February as the simulated downsloping winds became shallower (Figs. 13g,h). This shift in the stability structure, which appears to reflect the evolving large-scale environment, may explain the different character of the downslope winds during the two phases. Vosper (2004) and Durran (1986) have demonstrated that the structure and intensity of windstorms can be very sensitive to even subtle shifts in characteristics such as inversion height and stable layer depth.

Figure 15 switches focus to the west–east vertical cross sections across SIL (see Fig. 12a), the focus of Fig. 6a. During the first phase of the event (Figs. 15a–d), the downslope winds were not able to progress beyond this station, at least at this latitude, prior to the afternoon retreat upslope. It is recalled that SIL's observed peak gust (41 m s^{-1}) occurred at 1820 UTC (Fig. 6a), the time of Fig. 15c. The winds extended farther downslope during the second pulse, fitfully forming jumplike features (Figs. 15e–g) in areas lacking stations (e.g., between BRM and SIL in Figs. 12e–g). The event winds waned more quickly in this portion of the central area than the subzone around WCK (Figs. 12h and 15h).

As seen earlier, SIL and BOC were among the most severely underpredicted sites (Fig. 9). Reconstructions for these two stations are very similar (Fig. 11e), which is unsurprising due to their small separation (1.6 km) relative to the 667-m resolution of D5. A nearby station, North Boulder Creek (NBC), was also underpredicted (Fig. 11f), with a delayed windstorm onset, although the model accurately captured the fact the NBC site was less windy than both SIL and BOC. At Barona Mesa (BRM), located farther downslope (Fig. 9), both the simulated and observed winds remained generally weak during the episode (Fig. 11g), suggesting that the model's rendition of the spatial extent of the strong winds is reasonable.

c. *Justification of the standard configuration*

Our standard configuration employs a sub-1-km nest placed over the heart of the SDG&E network. It is well appreciated that terrain gap and downslope flows are significantly modulated by the shape of the topography, which is in turn dependent on the resolution of the model grid and the topographic database. Horizontal resolution sensitivity is demonstrated using vertical cross sections taken west–east across station WCK for PX–ACM2 simulations employing horizontal grid spacings between 667 and 10 km (Fig. 16). The fields shown are 4-h averages taken between 1500 and 1900 UTC 15 February, straddling the peak of the event's first phase at WSY (Fig. 6b), and network- and event-averaged bias and MAE are also reported.

The previously noted jump over WCK (Fig. 13b) is revealed to be a persistent feature in the highest-resolution run (Fig. 16a), which also has the smallest bias and MAE of the four simulations shown. Although it does not capture the jump, the 2-km simulation (Fig. 16b) does resemble a spatially smoothed version of the 667-m run's flow, and the strongest winds are still correctly positioned near station WSY. Further resolution

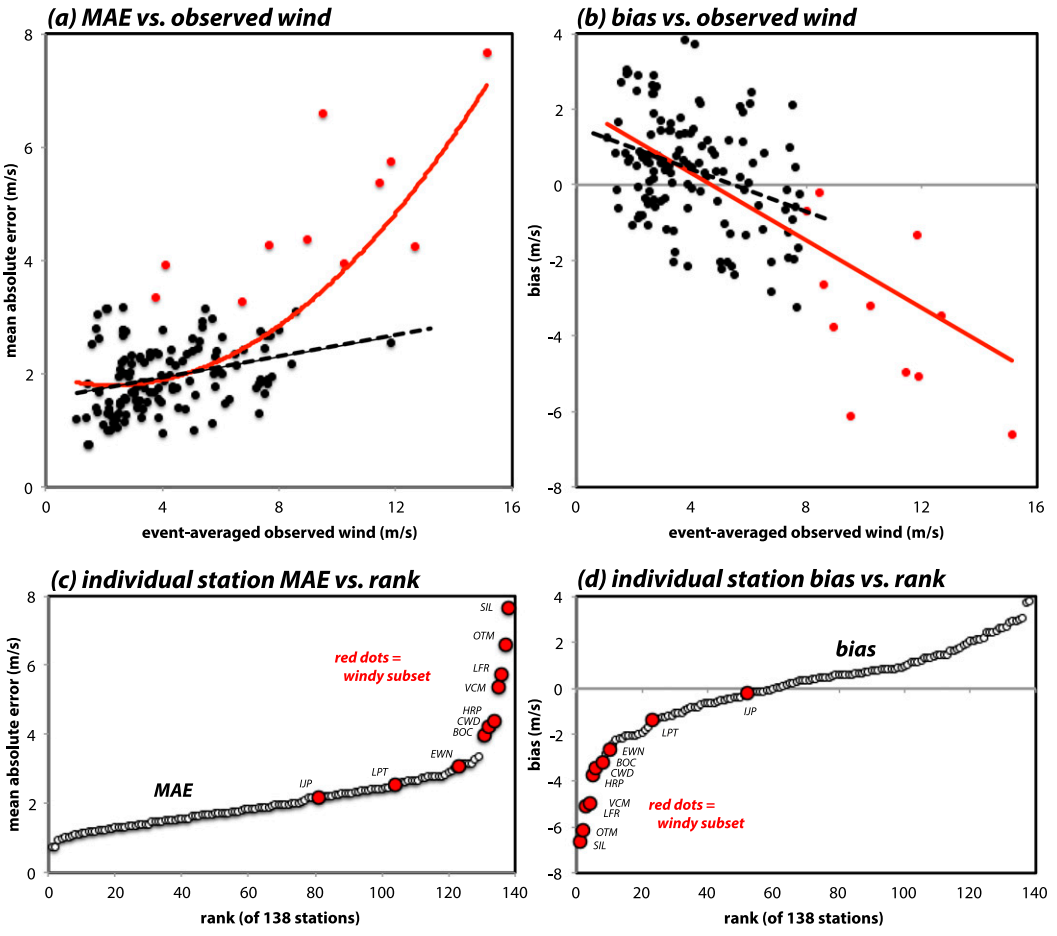

FIG. 10. (a) Scatterplot of event-mean observed wind vs MAE in the PX–ACM2 simulation for the 138 SDG&E stations. Red points identify the 10 windiest stations (see text). Least squares fits including all stations are shown in red, and those including only the black points are shown in black. (b) As in (a), but for event-mean observed wind vs mean bias. (c) Station MAE shown in rank order, with red points again identifying the windiest stations (identified by name). (d) As in (c), but for bias.

degradation, however, profoundly alters the shape of the terrain and improperly changes the location and horizontal extent of the maximum winds, leading to larger MAEs and sizable high wind biases (Figs. 16c,d). (Recall from the introduction that operational models tended to push high winds too far down the slope too often; clearly lower resolution can contribute to that.) Based on these results, it is concluded that 2-km resolution is acceptable but wider grid spacing cannot reliably place the fastest winds at the most likely correct locations. We elected to deploy a sub-1-km domain within the SDG&E mesonet to capture relatively subtle features such as the narrow northeast–southwest-oriented canyon immediately east of WSY and the terrain depression near WCK that can be seen in Fig. 16a.

As mentioned earlier, PX–ACM2 was selected for the standard run owing to its small MAE and nearly zero bias for the event-averaged sustained wind, in this as well as other cases (cf. Cao 2015, and below). Nearly all other physics combinations resulted in a positive wind bias as well as larger MAE for this event (Fig. 17). The members have clearly clustered with respect to LSM, with the choice of the PBL scheme having only a secondary effect (especially after the cosmetic MYJ–QNSE fix; see section 2c). For a given LSM, we have often found the largest error to be associated with the TEMF PBL parameterization, as also occurred in this experiment. This is believed to be another cosmetic result, being a consequence of TEMF's surface layer scheme not incorporating stability corrections [ψ in Eq. (1)] into its near-surface wind diagnostic, thereby rendering it slightly less competitive relative to the alternatives. Keep in mind that these winds have been adjusted to the 6.1-m level; a straight comparison with the model's 10-m wind diagnostic would have suggested even larger overpredictions.

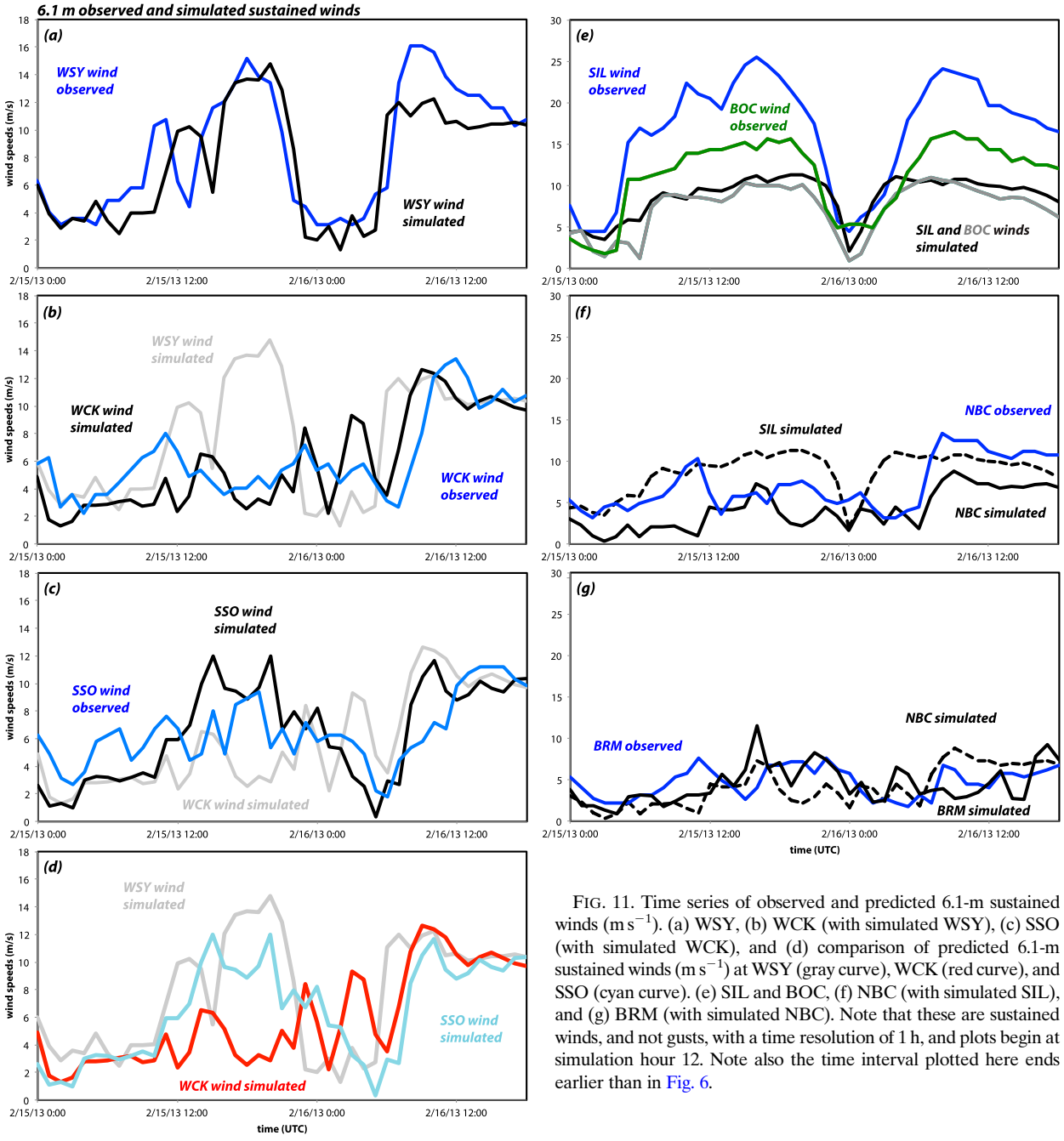

FIG. 11. Time series of observed and predicted 6.1-m sustained winds ($m\,s^{-1}$). (a) WSY, (b) WCK (with simulated WSY), (c) SSO (with simulated WCK), and (d) comparison of predicted 6.1-m sustained winds ($m\,s^{-1}$) at WSY (gray curve), WCK (red curve), and SSO (cyan curve). (e) SIL and BOC, (f) NBC (with simulated SIL), and (g) BRM (with simulated NBC). Note that these are sustained winds, and not gusts, with a time resolution of 1 h, and plots begin at simulation hour 12. Note also the time interval plotted here ends earlier than in Fig. 6.

The commonly employed Noah–YSU combination resided in the middle of our 48-member physics ensemble (Fig. 17), with obviously larger MAE at most stations (Fig. 8c). While SIL was still substantially underpredicted (Fig. 8d), over three-quarters of the sites had a positive wind bias (Fig. 18b). We note that this Noah–YSU run's bias and MAE were comparable to PX–ACM2's values from its 6-km run (see Fig. 16c).

Earlier, we demonstrated (Fig. 10) that while the network-averaged bias was nearly zero, the standard PX–ACM2 simulation's bias (and MAE) were functions of observed event-average sustained wind speed, driven primarily by a handful of particularly windy locations. Figure 18, which compares the PX–ACM2 configuration with two others, Noah–YSU and TD–TEMF, for the present as well as two other strong Santa Ana wind episodes, shows this tendency is a common occurrence. For

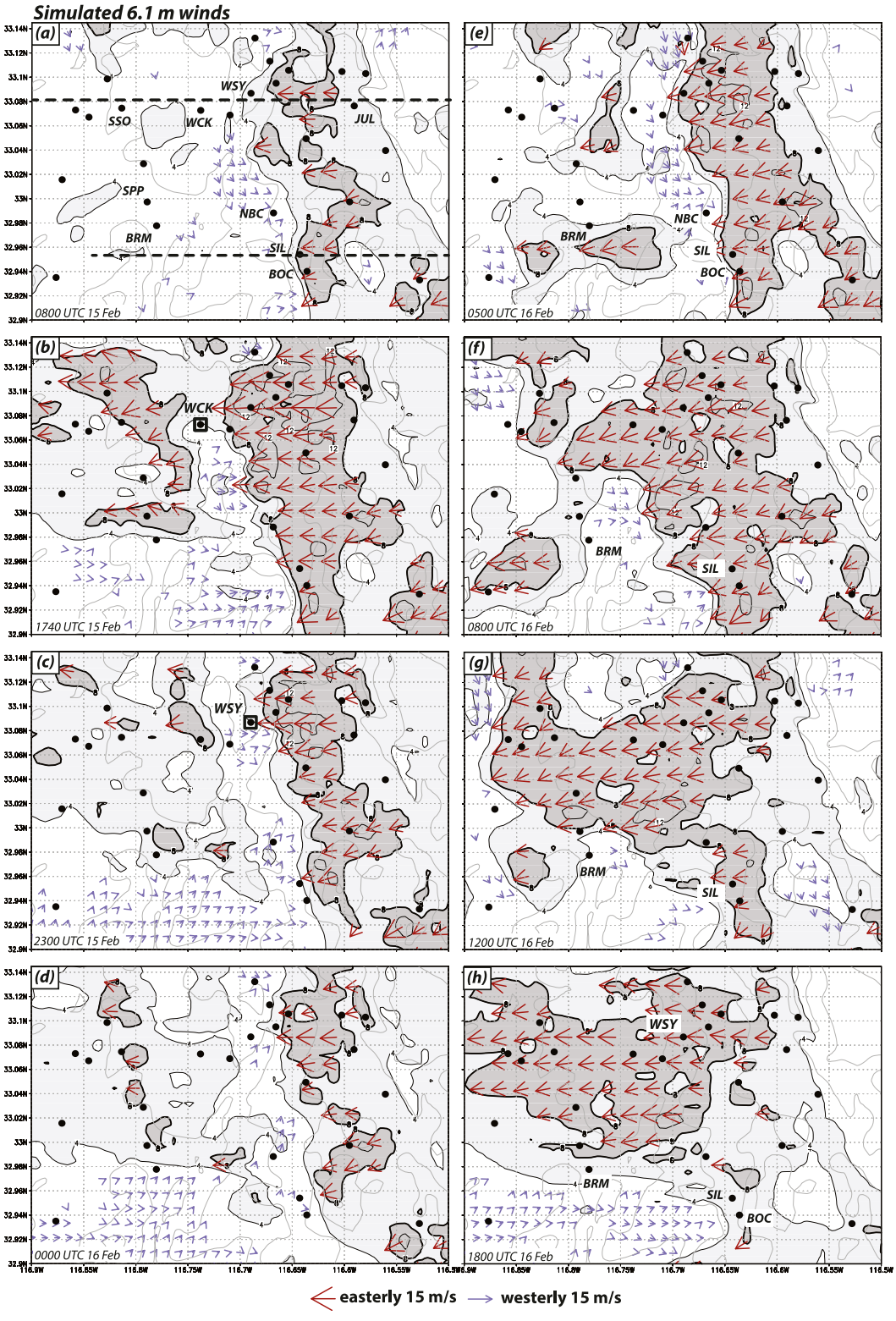

FIG. 12. Simulated 6.1-m horizontal wind speed (4 m s^{-1} interval, 8 m s^{-1} contour bolded) for (a) 0800 UTC 15 Feb, (b) 1740 UTC 15 Feb, (c) 2300 UTC 15 Feb, (d) 0000 UTC 16 Feb, (e) 0500 UTC 16 Feb, (f) 0800 UTC 16 Feb, (g) 1200 UTC 16 Feb, and (h) 1800 UTC 16 Feb 2013, with topography (300-m gray contours). Black dots denote SDG&E surface stations. Dashed lines in (a) denote locations of vertical cross sections shown in Figs. 13 and 15. Blue arrows denote winds with a westerly component ≥0.5 m s^{-1}, and red arrows denote winds with an easterly component ≥8 m s^{-1}. Many vectors are omitted for clarity.

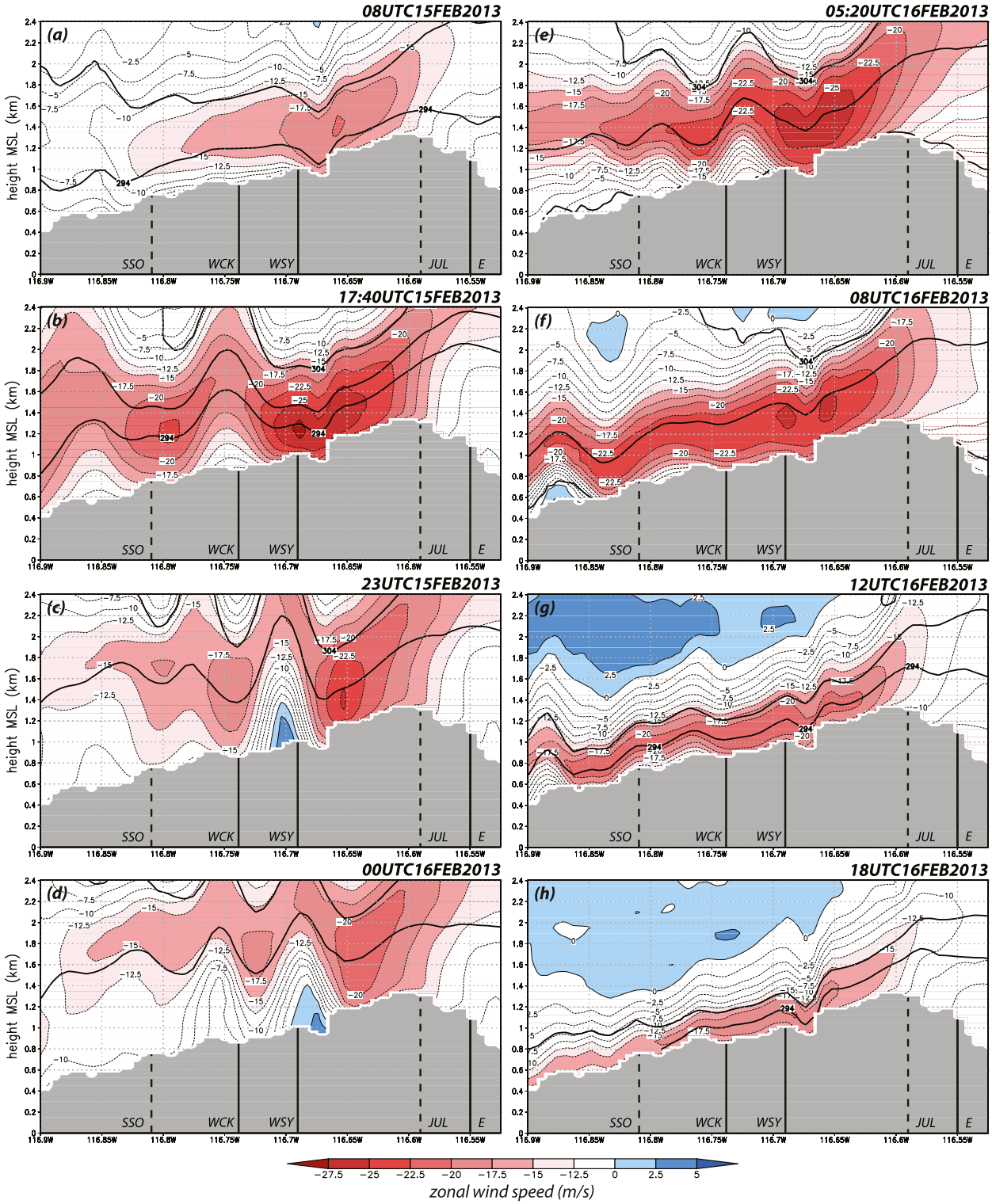

FIG. 13. Vertical cross section of zonal wind speed (shaded, with 2.5 m s^{-1} interval thin contours), taken west–east across WSY with underlying topography in gray (see Fig. 12a). Thick contours denote isentropes (5-K interval). Approximate locations of stations JUL, WSY, WCK, and SSO are marked. WCK, SSO, and JUL are displaced somewhat from the vertical plane depicted. The location for Fig. 14 is marked "E."

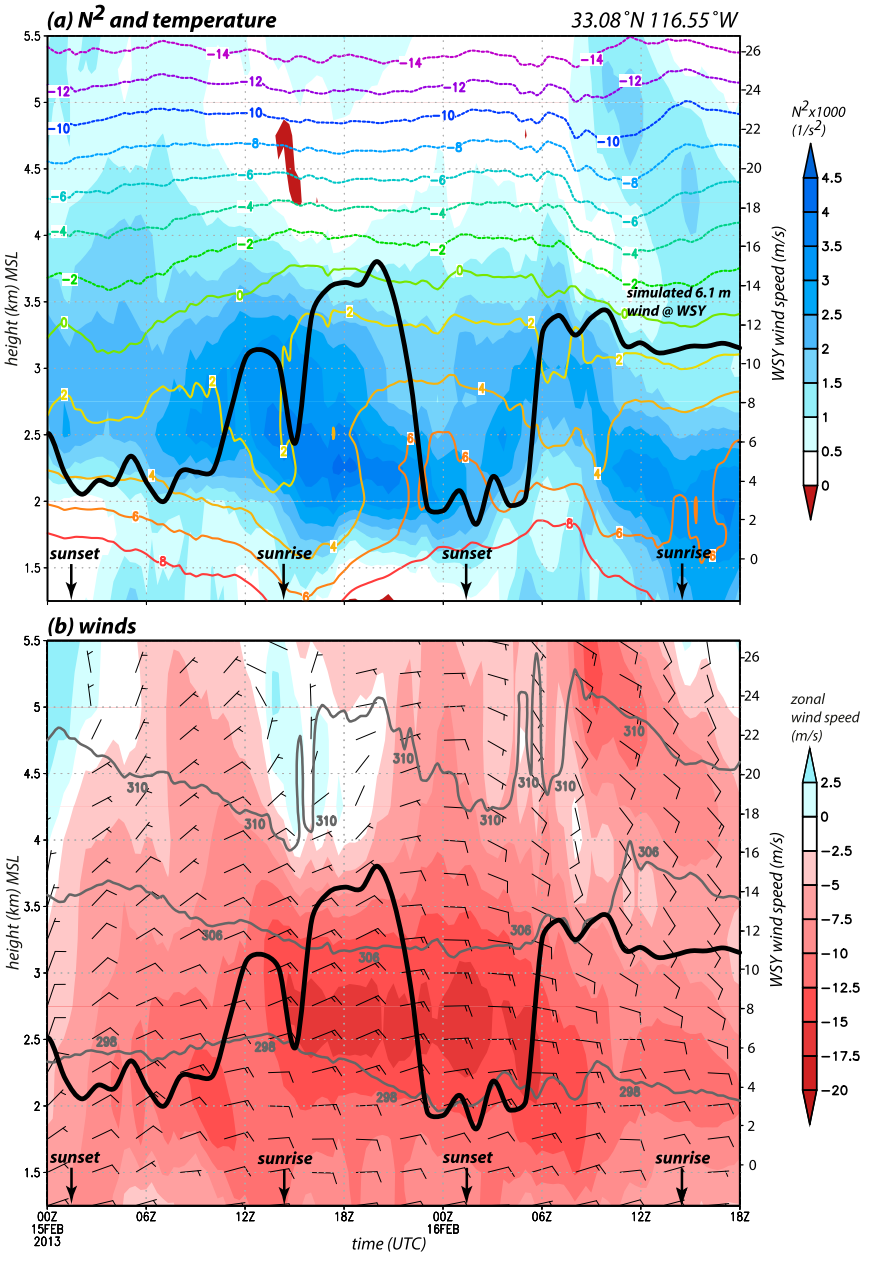

FIG. 14. Time–height plot of simulated (a) stability (dry squared Brunt–Väisälä frequency N^2, shaded as indicated) and temperature (2°C contours); and (b) zonal winds (shaded as indicated), horizontal wind barbs (in m s^{-1}), and selected potential temperature contours (298, 306, and 310 K) for location marked "E" in Fig. 13. Simulated sustained winds at WSY from Fig. 11a superposed for convenience; scale at right. Note that the plot does not start at model initiation time and fields have been vertically interpolated and thus wind barbs do not necessarily correspond to model levels.

PX–ACM2, aggregation of the three events still yields a roughly zero network-average bias, whether or not the windy subset is removed. The other two configurations, however, tend to have larger biases (e.g., TD–TEMF overpredicts the wind at over 80% of the stations among the three events) even before the windiest stations are removed, as well as larger spreads.

5. Discussion and summary

We have examined the 14–16 February 2013 Santa Ana event, which possessed many characteristics of a moderately intense downslope windstorm on the west-facing slopes of San Diego County, as part of an effort to improve wind forecast skill in this area. This study was made possible by observations from the San Diego Gas

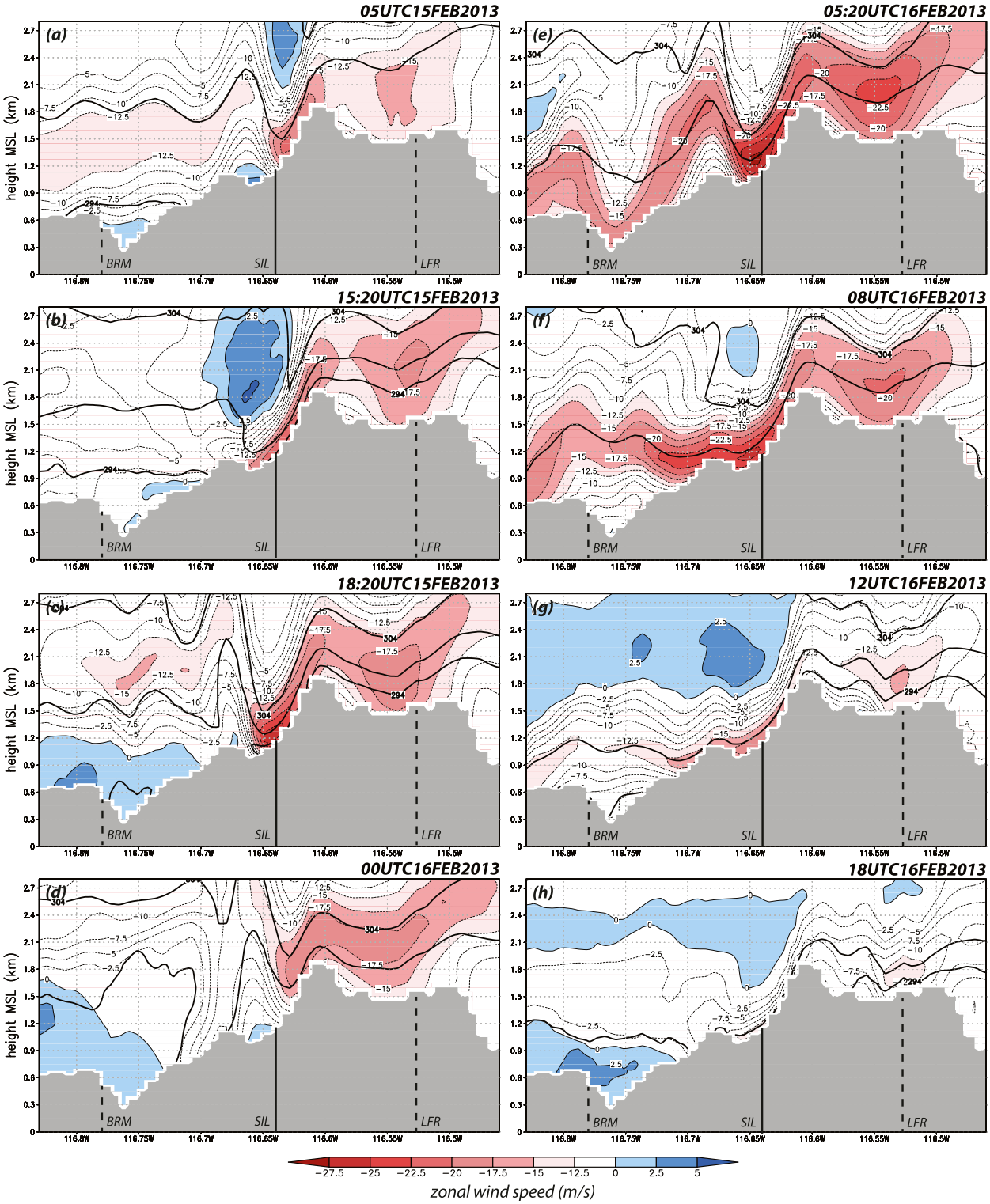

FIG. 15. As in Fig. 13, but across station SIL. Note that some times do not match those in Figs. 13a–h.

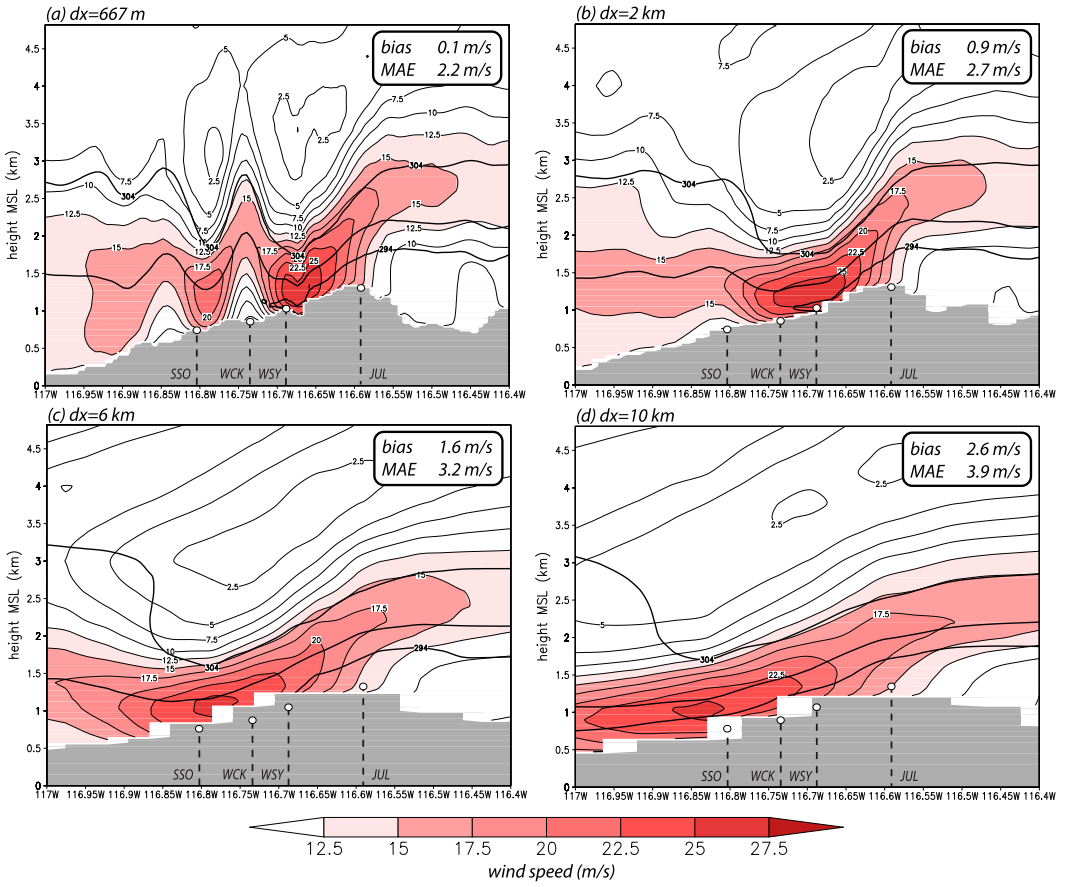

FIG. 16. Vertical cross sections of 4-h averaged horizontal wind speed (2.5 m s^{-1} contours and red shaded fields) for 1500–1900 UTC 15 Feb 2013, taken west–east across Witch Creek for the (a) 667-, (b) 2-, (c) 6-, and (d) 10-km horizontal grid spacing simulations. Thick black contours are the 294-, 299-, and 304-K isentropes. Gray shaded area depicts topography. The network- and event-averaged sustained wind MAE and bias are given in the box. The local rise in topography around 116.5°W longitude in the 2-km rendition results from a nearby topographic feature encroaching into the plane depicted owing to smoothing.

and Electric (SDG&E) mesonet, an unprecedented dense, homogeneous, and reliable observation network of ~140 stations sited in wind-prone areas, especially in the mountainous backcountry of San Diego County. These observations revealed that the 14–16 February 2013 Santa Ana episode consisted of two pulses separated by a protracted lull, and suggested that the first phase possessed a hydraulic jumplike flow in part of the network, while the second was characterized by a clear downslope progression of the winds with time as the event itself wound down.

The motivation of this study was to improve wind forecast skill in the area, and the WRF was selected for this effort. WRF provides many PBL and land surface parameterizations, permitting a very wide range of model configurations, many of which were tested for this and other recent Santa Ana wind events. Simulations were verified against SDG&E sustained wind observations, and the principal tools employed were the mean absolute error (MAE) and bias (mean error), averaged over the event at each station, and also averaged over the entire network. For this and other events, the Pleim–Xiu LSM with the ACM2 PBL scheme (PX–ACM2) combination performed well, typically minimizing MAE with a nearly zero bias with respect to the sustained wind when averaged over the network and event.

Telescoping nests were used with horizontal grid spacing of 2 km over San Diego County and 667 m over the county's highest terrain. While the 667-m grid permitted the model to capture the observed jumplike flow feature during the first pulse that was missing in the 2-km simulations, it otherwise had little influence on the network-averaged verification statistics. Horizontal resolution coarser than 2 km, however, exaggerated the spatial extent of the downslope flow, resulting in higher wind biases. Resolution also influences how well models

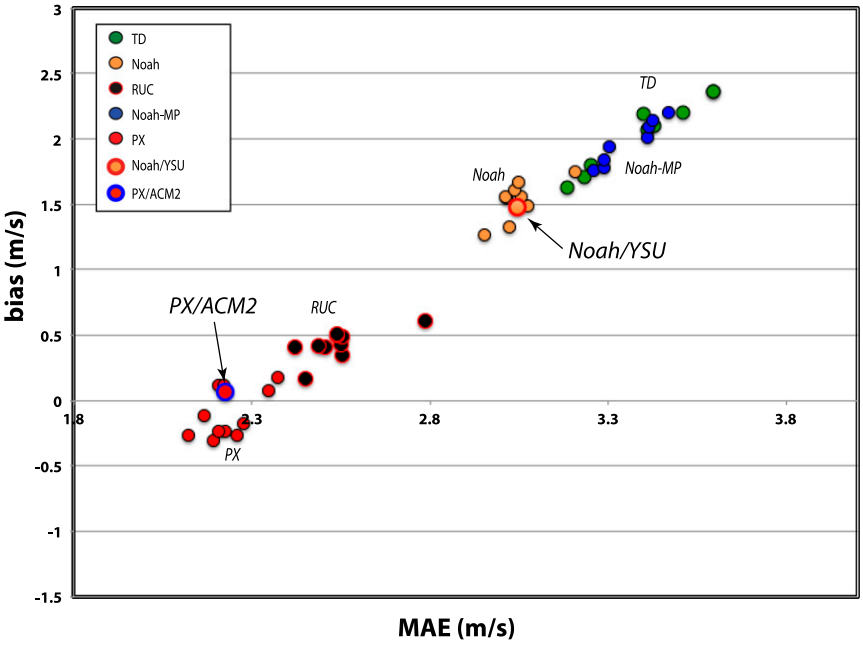

FIG. 17. Scatterplot of network- and event-averaged 6.1-m sustained wind bias vs MAE (both $m\,s^{-1}$) from the 48 physics ensemble members for the 14–16 Feb 2013 episode, color coded by LSM. For each PBL scheme, the recommended and/or most frequently adopted surface layer parameterization was employed. For members using the MYJ PBL scheme, a standard but cosmetic recalculation of the near-surface winds was removed, as noted in text. Horizontal diffusion option is turned off. The land-use database is derived from MODIS.

can capture other aspects of terrain-induced flow (e.g., Jackson et al. 2013; Reinecke and Durran 2009b) as well.

Even with adequate resolution, nearly all model configurations were found to consistently overpredict the winds at most stations in the SDG&E network, despite the adjustments for the nonstandard anemometer height (6.1 m AGL) that were made. Although it could be anticipated that the boundary layer was an important contributor (e.g., Smith 2007), this result was driven largely by the land surface model (LSM). Even the PX–ACM2 configuration had some issues, including possessing larger MAEs for windier stations, and the tendency to simultaneously overpredict less windy sites and underpredict flow speeds in windier areas of the network. In other words, the bias itself was biased. Other physics combinations, including the popular Noah–YSU configuration, resulted in a similar wind speed-dependent bias, just superposed on a larger, positive network-average mean error.

We infer from these results that event-averaged station bias represents the convolution of correctable and inherent errors, and that the PX–ACM2 combination has minimized the former relative to other configurations. In the next part of this study, we pursue the idea that the inherent error represents very small-scale influences that cannot possibly be resolved, even on a 667-m grid, features that permit the wind to vary over such small scales as previously discussed in the context of Fig. 5b. Part II will also explain why some LSMs outperformed others with respect to wind forecast skill.

It remains, however, that the PX–ACM2 simulation did a reasonable job of capturing the evolution and characteristics of this event. The model was then used to fill in gaps in the observations, especially the vertical structure of the wind field. Vertical cross sections revealed that the aforementioned jumplike feature did form on the west-facing slope, and did appear to be a hydraulic jump with reversed (upslope) near-surface flow. As observed, the simulated jump subsequently progressed upslope during the conclusion of the first phase of the event. The model also showed that while the winds were observed to be weak across the network during the afternoon lull, they actually stayed relatively strong near the ridgeline, in an area largely devoid of stations. Also captured by the model was the more uniform downslope flow that occurred during the event's second phase. These variations are of interest to local meteorologists as they help them understand what kinds of winds can occur at various places and times.

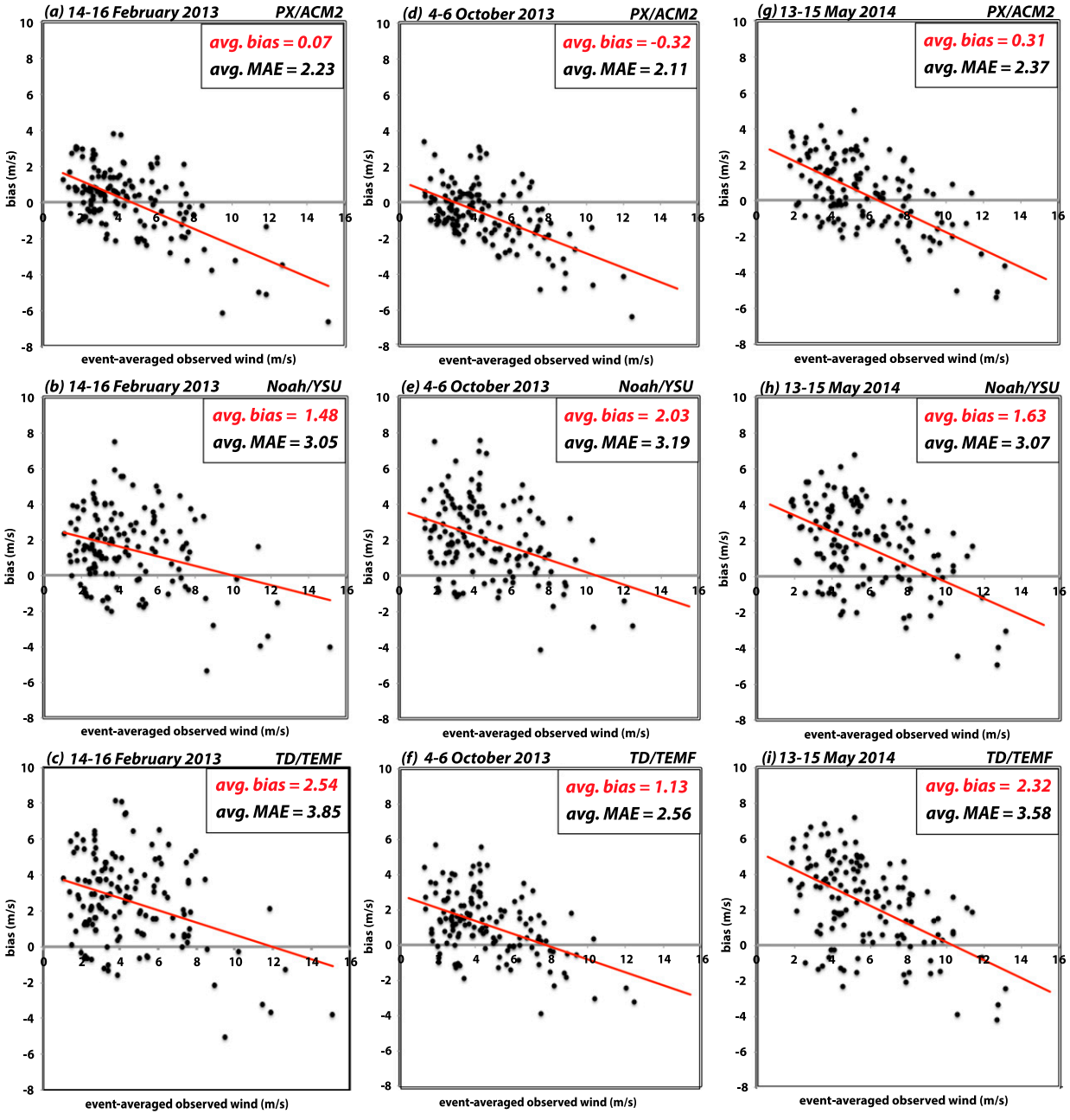

FIG. 18. Scatterplots of event-mean observed wind vs bias for SDG&E stations for three different Santa Ana wind events (columns), and three different LSM/PBL configurations (rows). A least squares fit (red line) is shown on each figure for reference. A version of (a) also appeared in Fig. 10.

Clearly, other variables such as temperature and humidity are also important for fire weather, and our experience has been that the Noah-based schemes, including Noah–MP (Niu et al. 2011), generally emerge as better with respect to MAE and bias (not shown). This motivates us to further investigate the difference among LSMs in predicting winds. Accordingly, the next part of this study will examine how and why model physics influences forecast skill with respect to the sustained winds, what needs to be done to the Noah-based schemes to improve their wind forecast skill, and will address the important issue of gust parameterization, as the greatest concern is the impact of these high-frequency, small-scale wind bursts that models of the present time cannot resolve. As in the present study, a key role will be played by the exceptionally dense and homogeneous SDG&E network.

Acknowledgments. This research was sponsored by the San Diego Gas and Electric Company. The authors thank Steve Vanderburg and Brian D'Agostino of San Diego Gas and Electric for their assistance and support. Travis Wilson designed many scripts involved in the verification, which employed the Model Evaluation Tools (MET) package from the Developmental Testbed Center. The authors would also like to acknowledge high-performance computing support from Yellowstone (ark:/85065/d7wd3xhc) provided by NCAR's Computational and Information Systems Laboratory, sponsored by the National Science Foundation. The authors thank the three anonymous reviewers for their constructive suggestions.

REFERENCES

Angevine, W. M., H. Jiang, and T. Mauritsen, 2010: Performance of an eddy diffusivity-mass flux scheme for shallow cumulus boundary layers. *Mon. Wea. Rev.*, **138**, 2895–2912, doi:10.1175/2010MWR3142.1.

Brinkmann, W. A. R., 1974: Strong downslope winds at Boulder, Colorado. *Mon. Wea. Rev.*, **102**, 592–602, doi:10.1175/1520-0493(1974)102<0592:SDWABC>2.0.CO;2.

Cao, Y., 2015: The Santa Ana Winds of Southern California in the context of fire weather. Ph.D. thesis, University of California, Los Angeles, 173 pp.

Chang, C.-H., and F. P. Schoenberg, 2011: Testing separability in marked multidimensional point processes with covariates. *Ann. Inst. Stat. Math.*, **63**, 1103–1122, doi:10.1007/s10463-010-0284-7.

Chanson, H., 2009: Current knowledge in hydraulic jumps and related phenomena. A survey of experimental results. *Eur. J. Mech.*, **28B**, 191–210, doi:10.1016/j.euromechflu.2008.06.004.

Chen, F., and J. Dudhia, 2001: Coupling an advanced land surface-hydrology model with the Penn State–NCAR MM5 modeling system. Part I: Model implementation and sensitivity. *Mon. Wea. Rev.*, **129**, 569–585, doi:10.1175/1520-0493(2001)129<0569:CAALSH>2.0.CO;2.

Doyle, J. D., and D. R. Durran, 2004: Recent developments in the theory of atmospheric rotors. *Bull. Amer. Meteor. Soc.*, **85**, 337–342, doi:10.1175/BAMS-85-3-337.

Durran, D. R., 1986: Another look at downslope windstorms. Part I: The development of analogs to supercritical flow in an infinitely deep, continuously stratified fluid. *J. Atmos. Sci.*, **43**, 2527–2527, doi:10.1175/1520-0469(1986)043<2527:ALADWP>2.0.CO;2.

——, 1990: Mountain waves and downslope winds. *Atmospheric Processes over Complex Terrain*, *Meteor. Monogr.*, No. 45, Amer. Meteor. Soc., 59–81.

——, 2003: Downslope winds. *Encyclopedia of Atmospheric Sciences*, G. North, J. Pyle, and F. Zhang, Eds., Elsevier Science, 644–650.

——, and J. B. Klemp, 1987: Another look at downslope winds. Part II: Nonlinear amplification beneath wave-overturning layers. *J. Atmos. Sci.*, **44**, 3402–3412, doi:10.1175/1520-0469(1987)044<3402:ALADWP>2.0.CO;2.

Ek, M. B., K. E. Mitchell, Y. Lin, E. Rogers, P. Grunmann, V. Koren, G. Gayno, and J. D. Tarpley, 2003: Implementation of Noah land surface model advances in the National Centers for Environmental Prediction operational mesoscale Eta model. *J. Geophys. Res.*, **108**, 8851, doi:10.1029/2002JD003296.

Hong, S.-Y., Y. Noh, and J. Dudhia, 2006: A new vertical diffusion package with an explicit treatment of entrainment processes. *Mon. Wea. Rev.*, **134**, 2318–2341, doi:10.1175/MWR3199.1.

Huang, C., Y. L. Lin, M. L. Kaplan, and J. J. Charney, 2009: Synoptic-scale and mesoscale environments conducive to forest fires during the October 2003 extreme fire event in Southern California. *J. Appl. Meteor. Climatol.*, **48**, 553–579, doi:10.1175/2008JAMC1818.1.

Hughes, M., and A. Hall, 2010: Local and synoptic mechanisms causing Southern California's Santa Ana winds. *Climate Dyn.*, **34**, 847–857, doi:10.1007/s00382-009-0650-4.

Iacono, M. J., J. S. Delamere, E. J. Mlawer, M. W. Shephard, S. A. Clough, and W. D. Collins, 2008: Radiative forcing by long-lived greenhouse gases: Calculations with the AER radiative transfer models. *J. Geophys. Res.*, **113**, D13103, doi:10.1029/2008JD009944.

Jackson, P. L., G. Mayr, and S. Vosper, 2013: Dynamically-driven winds. *Mountain Weather Research and Forecasting*, F. K. Chow, S. F. J. D. Wekker, and B. J. Snyder, Eds., Springer-Verlag, 121–218.

Janjić, Z. I., 1994: The step-mountain Eta coordinate model: Further developments of the convection, viscous sublayer, and turbulence closure schemes. *Mon. Wea. Rev.*, **122**, 927–945, doi:10.1175/1520-0493(1994)122<0927:TSMECM>2.0.CO;2.

Jones, C., F. Fujioka, and L. M. V. Carvalho, 2010: Forecast skill of synoptic conditions associated with Santa Ana winds in Southern California. *Mon. Wea. Rev.*, **138**, 4528–4541, doi:10.1175/2010MWR3406.1.

Klemp, J. B., and D. R. Lilly, 1975: The dynamics of wave-induced downslope winds. *J. Atmos. Sci.*, **32**, 320–339, doi:10.1175/1520-0469(1975)032<0320:TDOWID>2.0.CO;2.

Mass, C. F., D. Ovens, K. Westrick, and B. A. Colle, 2002: Does increasing horizontal resolution produce more skillful forecasts? *Bull. Amer. Meteor. Soc.*, **83**, 407–430, doi:10.1175/1520-0477(2002)083<0407:DIHRPM>2.3.CO;2.

National Wildfire Coordinating Group, 2014: Interagency Wildland Fire Weather Station Standards and Guidelines (PMS 426-3). National Wildfire Coordinating Group, 52 pp. [Available online at http://www.nwcg.gov/publications/interagency-wildland-fire-weather-station-standards-and-guidelines.]

Niu, G.-Y., and Coauthors, 2011: The community Noah land surface model with multiparameterization options (Noah-MP): 1. Model description and evaluation with local-scale measurements. *J. Geophys. Res.*, **116**, D12109, doi:10.1029/2010JD015139.

NOAA, 1998: Automated Surface Observing System (ASOS) user's guide. National Oceanic and Atmospheric Administration, 72 pp. [Available online at http://www.nws.noaa.gov/asos/pdfs/aum-toc.pdf.]

Oke, T. R., 1987: *Boundary Layer Climates.* Routledge, 435 pp.

Peltier, W. R., and T. L. Clark, 1979: The evolution and stability of finite-amplitude mountain waves. Part II: Surface wave drag and severe downslope windstorms. *J. Atmos. Sci.*, **36**, 1498–1529, doi:10.1175/1520-0469(1979)036<1498:TEASOF>2.0.CO;2.

Pleim, J. E., 2007a: A combined local and nonlocal closure model for the atmospheric boundary layer. Part I: Model description and testing. *J. Appl. Meteor. Climatol.*, **46**, 1383–1395, doi:10.1175/JAM2539.1.

——, 2007b: A combined local and nonlocal closure model for the atmospheric boundary layer. Part II: Application and evaluation in a mesoscale meteorological model. *J. Appl. Meteor. Climatol.*, **46**, 1396–1409, doi:10.1175/JAM2534.1.

——, and A. Xiu, 1995: Development and testing of a surface flux and planetary boundary layer model for application in mesoscale models. *J. Appl. Meteor.*, **34**, 16–32, doi:10.1175/1520-0450-34.1.16.

Raphael, M., 2003: The Santa Ana winds of California. *Earth Interact.*, **7**, doi:10.1175/1087-3562(2003)007<0001:TSAWOC>2.0.CO;2.

Reinecke, P. A., and D. R. Durran, 2009a: Initial-condition sensitivities and the predictability of downslope winds. *J. Atmos. Sci.*, **66**, 3401–3418, doi:10.1175/2009JAS3023.1.

——, and ——, 2009b: The overamplification of gravity waves in numerical solutions to flow over topography. *Mon. Wea. Rev.*, **137**, 1533–1549, doi:10.1175/2008MWR2630.1.

Schamp, H., 1964: *Die Winde der Erde und ihre Namen (The Winds of the Earth and Their Names)*. Franz Steiner Verlag, 94 pp.

Sheridan, P. F., and S. B. Vosper, 2006: A flow regime diagram for forecasting lee waves, rotors and downslope winds. *Meteor. Appl.*, **13**, 179–195, doi:10.1017/S1350482706002088.

Shin, H. H., S. Y. Hong, and J. Dudhia, 2012: Impacts of the lowest model level height on the performance of planetary boundary layer parameterizations. *Mon. Wea. Rev.*, **140**, 664–682, doi:10.1175/MWR-D-11-00027.1.

Skamarock, W. C., and Coauthors, 2008: A description of the Advanced Research WRF version 3. Tech. Note NCAR/TN-475+STR, 113 pp., doi:10.5065/D68S4MVH.

Small, I. J., 1995: Santa Ana winds and the fire outbreak of fall 1993. NOAA Tech. Memo., National Oceanic and Atmospheric Administration, National Weather Service Scientific Services Division, Western Region, 30 pp. [NTIS PB-199520.]

Smith, R. B., 2007: Interacting mountain waves and boundary layers. *J. Atmos. Sci.*, **64**, 594–607, doi:10.1175/JAS3836.1.

——, J. D. Doyle, Q. Jiang, and S. A. Smith, 2007: Alpine gravity waves: Lessons from MAP regarding mountain wave generation and breaking. *Quart. J. Roy. Meteor. Soc.*, **133**, 917–936, doi:10.1002/qj.103.

Sommers, W. T., 1978: LFM forecast variables related to Santa Ana wind occurrences. *Mon. Wea. Rev.*, **106**, 1307–1316, doi:10.1175/1520-0493(1978)106<1307:LFVRTS>2.0.CO;2.

Stensrud, D. J., 2007: *Parameterization Schemes: Keys to Understanding Numerical Weather Prediction Models.* Cambridge University Press, 488 pp.

Sukoriansky, S., B. Galperin, and V. Perov, 2006: A quasi-normal scale elimination model of turbulence and its application to stably stratified flows. *Nonlinear Processes Geophys.*, **13**, 9–22, doi:10.5194/npg-13-9-2006.

Tyner, B., A. Aiyyer, J. Blaes, and D. R. Hawkins, 2015: An examination of wind decay, sustained wind speed forecasts, and gust factors for recent tropical cyclones in the mid-Atlantic region of the United States. *Wea. Forecasting*, **30**, 153–176, doi:10.1175/WAF-D-13-00125.1.

Verkaik, J. W., 2000: Evaluation of two gustiness models for exposure correction calculations. *J. Appl. Meteor.*, **39**, 1613–1626, doi:10.1175/1520-0450(2000)039<1613:EOTGMF>2.0.CO;2.

Vosper, S. B., 2004: Inversion effects on mountain lee waves. *Quart. J. Roy. Meteor. Soc.*, **130**, 1723–1748, doi:10.1256/qj.03.63.

Wei, H., M. Segal, W. J. Gutowski, Z. Pan, R. W. Arritt, and J. W. A. Gallus, 2001: Sensitivity of simulated regional surface thermal fluxes during warm advection snowmelt to selection of the lowest model level height. *J. Hydrometeor.*, **2**, 395–406, doi:10.1175/1525-7541(2001)002⟨0395:SOSRST⟩2.0.CO;2.

Westerling, A. L., D. R. Cayan, T. J. Brown, B. L. Hall, and L. G. Riddle, 2004: Climate, Santa Ana winds and autumn wildfires in Southern California. *Eos, Trans. Amer. Geophys. Union*, **85**, 289–296, doi:10.1029/2004EO310001.

Wieringa, J., 1976: An objective exposure correction method for average wind speeds measured at a sheltered location. *Quart. J. Roy. Meteor. Soc.*, **102**, 241–253, doi:10.1002/qj.49710243119.

WMO, 2010: Guide to Meteorological Instruments and Methods of Observation. WMO Rep. 8, Secretariat of the WMO (World Meteorological Organization), Geneva, Switzerland, 716 pp.

Xiu, A., and J. E. Pleim, 2001: Development of a land surface model. Part I: Application in a mesoscale meteorological model. *J. Appl. Meteor.*, **40**, 192–209, doi:10.1175/1520-0450(2001)040<0192:DOALSM>2.0.CO;2.

Yoshino, M. M., 1975: *Climate in a Small Area: An Introduction to Local Meteorology.* University of Tokyo Press, 549 pp.

Zängl, Z., A. Gohm, and F. Obleitner, 2008: The impact of the PBL scheme and the vertical distribution of model layers on simulations of Alpine foehn. *Meteor. Atmos. Phys.*, **99**, 105–128, doi:10.1007/s00703-007-0276-1.